Water Resources Research

RESEARCH ARTICLE
10.1029/2023WR034605

Special Section:
Impacts on Water Resources of Coupled Hydrological, Chemical, and Mechanical Processes in the Fractured Subsurface

Phase-Field Simulations of Epitaxial Crystal Growth in Open Fractures With Reactive Lateral Flow

Michael Späth[1], Michael Selzer[1,2], Benjamin Busch[3], Daniel Schneider[1,2], Christoph Hilgers[3], Janos L. Urai[4], and Britta Nestler[1,2,5]

[1]Institute of Nanotechnology (INT), Karlsruhe Institute of Technology (KIT), Karlsruhe, Germany, [2]Institute of Digital Materials Science (IDM), Karlsruhe University of Applied Sciences, Karlsruhe, Germany, [3]Institute of Applied Geosciences - Structural Geology & Tectonics (AGW-SGT), Karlsruhe Institute of Technology (KIT), Karlsruhe, Germany, [4]Institute of Tectonics and Geodynamics, RWTH Aachen University, Aachen, Germany, [5]Institute for Applied Materials (IAM-MMS), Karlsruhe Institute of Technology (KIT), Karlsruhe, Germany

Key Points:

- Reactive fluid flow with advective mass transfer causes locally variable precipitation rate in open fracture
- A higher flow velocity or a higher supersaturation results in faster precipitation along the flow channel
- Phase-field modeling allows reproduction of laboratory crystal growth experiments from an advecting fluid using transmitted light microscopy

Correspondence to:
M. Späth,
michael.spaeth@kit.edu

Citation:
Späth, M., Selzer, M., Busch, B., Schneider, D., Hilgers, C., Urai, J. L., & Nestler, B. (2023). Phase-field simulations of epitaxial crystal growth in open fractures with reactive lateral flow. *Water Resources Research*, *59*, e2023WR034605. https://doi.org/10.1029/2023WR034605

Received 3 FEB 2023
Accepted 22 JUL 2023

© 2023. The Authors.
This is an open access article under the terms of the Creative Commons Attribution-NonCommercial-NoDerivs License, which permits use and distribution in any medium, provided the original work is properly cited, the use is non-commercial and no modifications or adaptations are made.

Abstract Fluid flow in fracture porosity in the Earth's crust is in general accompanied by crystallization or dissolution depending on the state of saturation. The evolution of the microstructure in turn affects the transport and mechanical properties of the rock, but the understanding of this coupled system is incomplete. Here, we aim to simulate spatio-temporal observations of laboratory experiments at the grain scale (using potash alumn), where crystals grow in a fracture during reactive flow, and show a varying growth rate along the fracture due to saturation differences. We use a multiphase-field modeling approach, where reactive fluid flow and crystal growth is computed and couple the chemical driving force for grain growth to the local saturation state of the fluid. The supersaturation of the fluid is characterized by a concentration field which is advected by fluid flow and in turn affects the crystal growth with anisotropic growth kinetics. The simulations exhibit good agreement with the experimental results, providing the basis for upscaling our results to larger scale computations of combined multi-physical processes in fractured porous media for applications as groundwater protection, geothermal, and hydrocarbon reservoir prediction, water recovery, or storing H_2 or CO_2 in the subsurface.

Plain Language Summary In the Earth's crust fluid flow can occur in fractured rock and depending on the composition of the fluid and physical conditions minerals can precipitate or dissolve. This affects the properties of the rock system and is for example, of interest to subsurface engineering applications. In this work we simulate observations of laboratory experiments at the grain scale, where crystals grow in an open fracture during fluid flow. In these experiments, the growth rate of the crystals varies along the fracture since the supersaturation of the fluid decreases due to the crystallization. We use a multiphase-field model for the numerical simulation of crystal growth in the open fracture and combine it with reactive fluid flow. With the presented model the driving force for grain growth is coupled to the local supersaturation, which enables the incorporation of reactive mass transport in open fractures. Our phase-field simulations agree with the laboratory experiments. The presented simulative approach can be used for upscaling the results on microscale to larger length and time scales and can help to better predict the subsurface behavior for example, of groundwater, fractured geothermal, and hydrocarbon reservoirs.

1. Introduction

Fluid flow in open fractures is a fundamental process in rock systems in the upper and middle crust. Dilatant fractures formed during deformation can induce fluid pathways relevant to pollutant transport, water production, wastewater storage, and geothermal applications. Depending on the chemical conditions of the aqueous fluid (e.g., supersaturation, chemical potential) crystal growth or dissolution processes can occur, which control different properties of the rock system (e.g., permeability, strength, solute transport, tortuosity). The evolving crystal structures in open dilation sites can contain information about the formation conditions, for example, deformation history or fluid pressure (Becker et al., 2011; Bons et al., 2012; Boullier & Robert, 1992; Cox, 2007; Fisher & Brantley, 1992). A deeper understanding of the coupled processes of fluid flow and crystallization is of great importance to various fields of water resources management and basic or applied geosciences, that is, injection and production of fluids from the subsurface, geothermal energy production, or storage of hydrogen, heat, or carbon dioxide (Almansour et al., 2020; Birkholzer et al., 2009; Cox et al., 1987; McNamara et al., 2016; Rutqvist, 2012; Sibson et al., 1988; Steefel et al., 2013).

Fluid flow in fractured subsurface environments can be steady or episodic (Sibson et al., 1975). Both diffusion and advection can play a major role in the transport of mass. The physical properties of the fluid (e.g., temperature, composition, velocity) affect the evolving microstructure such as the ratio of advective to diffusive mass transport, degree of supersaturation, mineralogical composition, crystal defects, or coatings. The relative importance of these processes can be described by characteristic dimensionless numbers such as the Péclet number, Damköhler number or the Reynolds number. The Péclet number describes the ratio between advective to diffusive mass transport, the Damköhler number Da_{II} indicates the importance of attachment kinetics to diffusive transport and the Reynolds number characterizes how strong the inertial forces are compared to the viscous forces in the mobile fluid. A higher flow velocity can increase the crystal growth due to an increased importance of the advective transport (less depleted solution in domain) or a reduction of the diffusional boundary layer thickness. The resulting complex evolution of vein structures contain information about the processes that occurred in these natural laboratories.

Laboratory hydrothermal flow-through experiments of fractured rock or artificially generated channels have been presented for various minerals which are present in the earth crust (Busch et al., 2021; Cecil & Heald, 1971; Hilgers & Urai, 2002; Hilgers et al., 2004; Lander et al., 2008; Lee & Morse, 1999; Lee et al., 1996; Nollet et al., 2006; Okamoto & Sekine, 2011; Okamoto et al., 2010; Singurindy & Berkowitz, 2005; Thomas et al., 1949). With the help of these experiments the temporal evolution of crystal growth can be visualized during different time steps under well-defined conditions and provide insight into the formation mechanisms of crystallization in single and multi-grain environments can be provided. For example, in polycrystalline setups the interaction of differently oriented crystals can be studied during the precipitation under various conditions. In the works of Lee et al. (1996) and Lee and Morse (1999) calcite growth in a flow channel was investigated under different supersaturations at room temperature on the centimeter scale. In their experiments the change of fluid properties (e.g., pH, supersaturation, alkalinity) was measured at the inlet and outlet of the channel, while also imaging the evolving crystal structure. Another approach of flow through experiments with potash alum ($KAl(SO_4)_2{\cdot}12H_2O$) was performed by Hilgers and Urai (2002), Hilgers et al. (2004), and Nollet et al. (2006), where different factors influencing the microstructure (e.g., flow velocity, saturation state) were investigated. Potash alum shows a comparatively fast growth rate at low temperature and has well known growth kinetics. This allows the observation of the evolving microstructure and effects of depleting supersaturation under smaller length scales and short experimental times. In addition, Hilgers et al. (2004) scaled up the results obtained from the laboratory experiments to natural quartz veins and indicated how the observed mechanisms can be linked to natural systems. Singurindy and Berkowitz (2005) presented laboratory experiments of calcite dissolution and gypsum precipitation in fractured carbonate rocks, while also measuring the hydraulic conductivity. Syntaxial quartz growth in open fractures was, for example, investigated by Okamoto and Sekine (2011), where termination of crystals and crystallographic orientation-controlled growth competition was observed. Laboratory crystal growth experiments provide insight into geological processes, however are restricted to shorter time scales (days to months) and might face problems in fully resolving (spatial and temporal) the present physical fields (e.g., temperature, supersaturation).

Besides the enhancements of laboratory crystal growth experiments, computational modeling of precipitation in open fractures has evolved as an important and versatile methodology for providing insights into the crystallization process or the evolution of fluid connectivity. One of the first works in the direction of crystal growth in open fractures was introduced by Urai et al. (1991). Later works within the sharp interface context like *Facet* (Zhang & Adams, 2002) or *Vein Growth* (Bons, 2001; Hilgers et al., 2001; Nollet et al., 2005) extended the modeling of crystal growth and investigated effects of several factors on the evolving microstructure. These early works were based on front-tracking algorithms and were solely applied to 2D structures with one growth front. Moreover, crystal growth has been modeled with the cellular automaton program *Prism2D* (Lander et al., 2008), which also has been applied to single and multi-grain systems (Gale et al., 2010; Lander & Laubach, 2015). In Lander and Laubach (2015) *Prism2D* was calibrated with laboratory crystal growth experiments to demonstrate the formation of various crystal structures in natural veins by also ensuring an accurate description of the growth kinetics.

In addition, the modeling of reactive flow interacting with the microstructure has advanced in the last couple of years, where various modeling techniques are applied to precipitation and/or dissolution processes and show promising results. For example, with finite volume-based approaches like in Molins et al. (2017) and Deng et al. (2022) or with a micro-continuum approach (Soulaine & Tchelepi, 2016) fluid flow, mass transport, and mineral evolution can be depicted for the modeling of crystal dissolution or precipitation processes on the pore-scale. Further, approaches based on the Lattice Boltzmann method (Prasianakis et al., 2018), Level-set

approaches (Li et al., 2007), phase-field approaches (Xu & Meakin, 2008; Xu et al., 2012), or SPH based methods (Tartakovsky et al., 2007) are applied to reactive flow in subsurface environments. For an overview of reactive flow modeling we refer to Steefel et al. (2015), Steefel (2019), Viswanathan et al. (2022) and for a detailed comparison of different numerical approaches treating mineral dissolution in a reactive flow we refer to the review article by Molins et al. (2020).

Over the last decades, the phase-field method has evolved as a powerful tool to model phase transition processes (Moelans et al., 2008; Nestler & Choudhury, 2011; Steinbach, 2013). Within the phase-field method the interfaces between different phases (e.g., grains, liquid) are described in a diffuse manner, which allows the treatment of moving boundary problems without additional interface tracking or utilizing remeshing algorithms. The phase-field method is widely used in material science and multi-physics simulations can be performed by incorporating additional fields as temperature, concentration, or mechanics. There is a broad field of applications for coupling the phase-field with a concentration field. Previously, this coupling has been applied, for example, to corrosion of steels (e.g., Mai et al., 2016), solidification of alloys (e.g., Steinmetz et al., 2018) including advective effects (e.g., Laxmipathy et al., 2019), polymer solutions (e.g., H. Zhang et al., 2021), charging of battery systems (e.g., Daubner et al., 2022), hydrogen fuel cells (e.g., Hoffrogge et al., 2021), and martensitic phase transformation (e.g., Schoof et al., 2019), just to name a few.

Recently, the phase-field method has also been applied in geological environments and enables various applications such as precipitation or dissolution (Bringedal et al., 2020; Prajapati et al., 2021; Ray et al., 2019; Xu & Meakin, 2008) processes in fractured rock or reservoirs. Various minerals which frequently occur in subsurface environments have been investigated in 2D or 3D like calcite (Prajapati et al., 2017; Prajapati, Selzer, Nestler, Busch, & Hilgers, 2018; Späth et al., 2021; Spruženiece et al., 2020, 2021) or quartz (Ankit et al., 2015; Prajapati, Abad Gonzalez, et al., 2020; Prajapati, Selzer, Nestler, Busch, Hilgers, & Ankit, 2018; Späth et al., 2022a, 2022b; Wendler et al., 2016). For precipitation in geological systems Hubert et al. (2009) proposed the incorporation of various equations for an accurate description of modeling crystal growth in open fractures by a coupling with a diffusion, temperature, and fluid flow equations. In addition, there are several works available investigating the crystal evolution due to precipitation or dissolution (Bringedal et al., 2020; Ray et al., 2019; Xu et al., 2012).

Besides modeling precipitation or dissolution solely on the pore or grain scale several works upscaled results from reactive microstructural simulations to larger scales (e.g., meter or kilometer) by using for example, asymptotic expansion or homogenization techniques (Bringedal et al., 2020; Choquet & Mikelić, 2009; Le Borgne et al., 2011; Li et al., 2006; Mikelić et al., 2006; Ray et al., 2019; Redeker et al., 2016). In the upscaling process the microstructural models can be used with a macroscopic model unidirectionally (weak coupling, by e.g., interpolation) or bidirectionally (strong coupling, e.g., microscopic calculations with macroscopic input). In addition to models describing reactive flow in porous space, chemical transport in fractured rock has been upscaled and applied to fracture networks (Cvetkovic & Gotovac, 2014; Painter et al., 2008; Yamashita & Kimura, 1990). These approaches can incorporate heterogeneities at the grain-scale in the modeling and allow that the insights obtained from the microstructural simulations (e.g., reaction rates, interaction between grains, mechanical properties) can be applied to larger scales and enable implications on long term behavior of subsurface rock structures, which is of interest to applied geosciences (e.g., reservoir scale).

Even though the phase-field modeling of crystal growth has been applied in previous studies to various subsurface systems and a reconstruction of natural microstructures was possible, an extension to supersaturation dependent crystal growth in multi-grain environments including crystallographic anisotropies and allowing the depiction of temporal and spatial variations of crystallization velocities has not been presented so far. This work aims to extend previous phase-field modeling studies (Ankit et al., 2015; Laxmipathy et al., 2019; Prajapati, Abad Gonzalez, et al., 2020; Späth et al., 2021) with the incorporation of advective and diffusive mass transport by solving concentration and fluid flow equations. This modeling approach enables a quantitative description of the crystal growth process of potash alum in an advective fluid and opens the door for future works in the direction of crystal growth processes in fractured rock and in upscaling the results to the reservoir scale.

2. Methods

In this work we utilize the phase-field method for modeling crystal growth in open fractures. The method allows the coupling of the crystal growth with a concentration evolution and fluid flow and enables the incorporation of

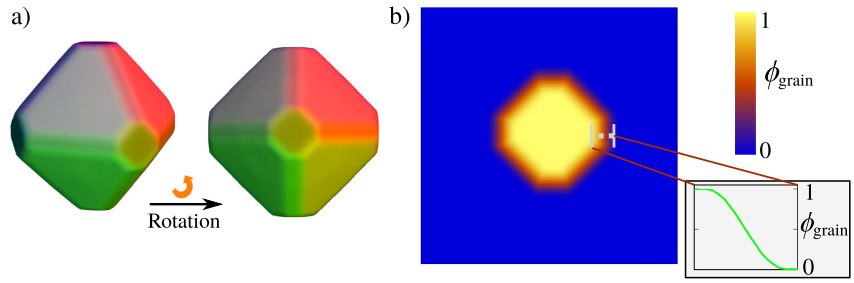

Figure 1. (a) Single potash alum crystal in 3D with {100}, {110}, and {111} facets. The 3D crystal is rotated and the 2D projection with {110} and {111} facets is used in the crystallization simulations. (b) Resulting 2D projection with diffuse interface between the crystal and liquid phase. The interface continuously decreases over its width in a sinusoidal profile (cut-out).

crystallographic anisotropies (Figure 1a). The presented multiphase-field model is based on the work of Nestler et al. (2005) and extends previous works of phase-field modeling of crystal growth in subsurface environments (e.g., Ankit et al., 2015; Prajapati, Abad Gonzalez, et al., 2020; Spruženiece et al., 2021; Wendler et al., 2016).

2.1. Multiphase-Field Model for Crystal Growth

We consider a domain Ω, in which N scalar-valued phase-field order parameters $\phi_\alpha(\boldsymbol{x}, t)$ are present and collect them into the phase-field tuple $\boldsymbol{\phi}(\boldsymbol{x}, t) = [\phi_1(\boldsymbol{x}, t), \ldots, \phi_N(\boldsymbol{x}, t)]$. Each phase-field parameter $\phi_\alpha(\boldsymbol{x}, t) \in [0, 1]$ describes the presence of a mineral crystal or the liquid phase at time t and position $\boldsymbol{x}$ in the domain Ω. The regions between different crystals or crystal states are characterized with a finite diffuse transition region, where the phase-field parameter ϕ_α increases continuously from zero where the crystal state is not present to one where the bulk phase is Figure 1b. The width of the diffuse interface region is controlled by the length scale parameter ϵ.

The phase-field model utilized in for example, Ankit et al. (2015), Prajapati, Selzer, Nestler, Busch, and Hilgers (2018), Prajapati, Abad Gonzalez, et al. (2020), Spruženiece et al. (2021), and Späth et al. (2021, 2022a) is extended to a concentration dependent driving force. This approach is based on the formulation of free energy density functional and enables the simulation of crystal growth rates dependent on the local saturation state. Instead of the free energy functional, here a grand potential energy functional (Choudhury & Nestler, 2012)

$$\Psi(\boldsymbol{\mu}, \boldsymbol{\phi}) = \int_\Omega \left(\epsilon a(\boldsymbol{\phi}, \nabla\boldsymbol{\phi}) + \frac{1}{\epsilon} w(\boldsymbol{\phi}) + \psi_{\text{bulk}}(\boldsymbol{\mu}, \boldsymbol{\phi}) \right) \mathrm{d}\Omega = \Psi_{\text{intf}} + \Psi_{\text{bulk}} \tag{1}$$

is used to include the chemical potential of the order parameter into the modeling (see discussion below). The functional comprises the terms of the gradient energy density $\epsilon a(\boldsymbol{\phi}, \nabla\boldsymbol{\phi})$, the potential energy density $w(\boldsymbol{\phi})/\epsilon$, and the grand potential density $\psi_{\text{bulk}}(\boldsymbol{\mu}, \boldsymbol{\phi}) = \sum_{\alpha=1}^{N} \psi_{\text{bulk}}^{\alpha}(\boldsymbol{\mu}) h^\alpha(\boldsymbol{\phi})$. The interfacial energy density contributions in Equation 1 are represented by the first two terms. For the potential energy density, a multi-obstacle type potential is used in this work, which is given by

$$\frac{w(\boldsymbol{\phi})}{\epsilon} = \begin{cases} \frac{16}{\epsilon\pi^2} \sum_{\alpha=1}^{N} \sum_{\beta>\alpha}^{N} \gamma_{\alpha\beta} \phi_\alpha \phi_\beta + \frac{1}{\epsilon} \sum_{\alpha=1}^{N} \sum_{\beta>\alpha}^{N} \sum_{\delta>\beta}^{N} \gamma_{\alpha\beta\delta} \phi_\alpha \phi_\beta \phi_\delta & \text{if } \boldsymbol{\phi} \in \mathcal{G} \\ \infty & \text{else,} \end{cases} \tag{2}$$

where $\mathcal{G} = \left\{ \boldsymbol{\phi} \middle| \sum_\alpha \phi_\alpha = 1, \text{and } \phi_\alpha \geq 0 \right\}$ is the Gibbs simplex. The second sum in Equation 2 impedes the occurrence of nonphysical contributions from minor phase-field variables by higher order terms $\sim\phi_\alpha\phi_\beta\phi_\delta$ in binary interface regions. With the gradient energy density, a prescription of a faceted crystal shape (e.g., Nestler et al., 2005) can be modeled and it is denoted by

$$\epsilon a(\boldsymbol{\phi}, \nabla\boldsymbol{\phi}) = \epsilon \sum_{\alpha=1}^{N} \sum_{\beta>\alpha}^{N} \gamma_{\alpha\beta} a_{\alpha\beta}^2(\boldsymbol{\phi}, \nabla\boldsymbol{\phi}) |\mathbf{q}_{\alpha\beta}|^2, \tag{3}$$

in which $\mathbf{q}_{\alpha\beta} = \phi_\alpha \nabla\phi_\beta - \phi_\beta \nabla\phi_\alpha$ is the generalized gradient and $\gamma_{\alpha\beta}$ is the interfacial energy of the α-β interface. Anisotropic crystal growth can be modeled with the gradient energy density function by adapting the factor $a_{\alpha\beta}(\boldsymbol{\phi}, \nabla\boldsymbol{\phi})$. A faceted type anisotropy is utilized by a piecewise defined anisotropic surface energy function

Table 1
Parameters for Crystal Growth of Potash Alum

Parameter	Value
Diffusivity D	5×10^{-10} m^2 s^{-1} (Nollet et al., 2006)
Supersaturation S	1.14 (Hilgers & Urai, 2002)
Surface energy $\gamma_{al.\text{-}liq.}$	2×10^{-3} J m^{-2} (Byrappa, 2003)
Bulk velocity u_b	1.6×10^{-4} m s^{-1} (Hilgers & Urai, 2002)
Temperature T	29.4°C (Hilgers & Urai, 2002)
Reynolds number	0.08 (Hilgers & Urai, 2002)
Solubility	15.35 g/100 gH_2O (Barrett & Glennon, 2002)
Péclet number	160 (Hilgers & Urai, 2002)
Mobility $M_{al.\text{-}liq.}$	5.4824×10^{-8} m^2 kg^{-1} s

$$a_{\alpha\beta}(\boldsymbol{\phi}, \nabla\boldsymbol{\phi}) = \max_{1\le k\le\zeta} \{\hat{\boldsymbol{n}} \cdot \eta_{k,\alpha\beta}\}, \tag{4}$$

with the normalized interface normal vector $\hat{\boldsymbol{n}} = \mathbf{q}_{\alpha\beta}/|\mathbf{q}_{\alpha\beta}|$. The kth vertex vector of the Wulff shape (total ζ vertex vectors) is denoted by $\eta_{k,\alpha\beta}$.

Besides the above discussed potential energy density and gradient energy density the functional includes a grand potential density

$$\psi_{\text{bulk}}(\boldsymbol{\mu}, \boldsymbol{\phi}) = \sum_{\alpha=1}^{N} \psi_{\text{bulk}}^{\alpha}(\boldsymbol{\mu}) h^{\alpha}(\boldsymbol{\phi}), \tag{5}$$

where $\psi_{\text{bulk}}^{\alpha}(\boldsymbol{\mu}) = f^{\alpha}(c^{\alpha}(\boldsymbol{\mu})) - \sum_{i=1}^{K-1} \mu_i c_i^{\alpha}(\boldsymbol{\mu})$ is the Legendre transformation of the free energy density. Therein, $\boldsymbol{\mu} = \{\mu_1, \ldots, \mu_K\}$ is the chemical potential of the K components in the system. The main assumption of this approach is that crystal states are in equilibrium when the chemical potentials are in equilibrium (Choudhury & Nestler, 2012).

The temporal evolution of each phase-field ϕ_α is related to the variational derivative of the grand potential energy (Equation 1) and is denoted by

$$\frac{\partial\phi_\alpha}{\partial t} = -\frac{1}{N\epsilon} \sum_{\substack{\beta=1 \\ \beta\neq\alpha}}^{N} \left[M_{\alpha\beta} \left(\frac{\delta\Psi_{\text{intf}}}{\delta\phi_\alpha} - \frac{\delta\Psi_{\text{intf}}}{\delta\phi_\beta} - \frac{8\sqrt{\phi_\alpha\phi_\beta}}{\pi} \left(\frac{\delta\Psi_{\text{bulk}}}{\delta\phi_\beta} - \frac{\delta\Psi_{\text{bulk}}}{\delta\phi_\alpha} \right) \right) \right] \tag{6}$$

in which $M_{\alpha\beta}$ is the mobility coefficient of the α-β interface. Here, the approach of Steinbach (2009) is used to obtain correct interface kinetics corresponding to the utilized obstacle-type potential energy density. This approach also avoids interpolation difficulties of the mobility in multiphase regions.

2.2. Diffusive and Advective Mass Transport

The driving force for the crystal evolution (Equation 5) is dependent on the local concentration field, for example, a higher or lower concentration than the solid state or crystal state-dependent equilibrium concentration $c_{\text{eq.}}^{\alpha}$ results in precipitation or dissolution respectively. The system comprises in general of K concentration components c_i, $i = 1..K$. The evolution equation for the $K-1$ independent chemical potentials is given by Choudhury and Nestler (2012)

$$\begin{aligned} \frac{\partial\mu_i}{\partial t} = & \sum_{i=1}^{K-1} \sum_{j=1}^{K-1} \left[\sum_{\alpha=1}^{N} h^{\alpha}(\boldsymbol{\phi}) \frac{\partial c_i^{\alpha}(\boldsymbol{\mu}, T)}{\partial\mu_j} \right]_{ij}^{-1} \\ & \times \left\{ \nabla \cdot \sum_{i=1}^{K-1} \sum_{j=1}^{K-1} (L_{ij}(\boldsymbol{\phi}, \boldsymbol{\mu}) \nabla\mu_j - \boldsymbol{u} c_i) - \sum_{\alpha=1}^{N} c_i^{\alpha}(\boldsymbol{\mu}, T) \frac{\partial h^{\alpha}(\boldsymbol{\phi})}{\partial t} \right\} \end{aligned} \tag{7}$$

with the interpolated diffusivities $L_{ij}(\boldsymbol{\phi}, \boldsymbol{\mu}) = \sum_{\alpha=1}^{N} h^{\alpha}(\boldsymbol{\phi}) D_{ij}^{\alpha} \left(\partial c_j^{\alpha}(\boldsymbol{\mu})/\partial\mu_j \right)$ (see e.g., Choudhury & Nestler, 2012) and the fluid velocity $\boldsymbol{u}$. The chemical potential field is advected by the fluid flow, which is computed by solving the incompressible Navier-Stokes equations. With the computed chemical potential, the resulting phase-specific concentration field c^{α} can be determined with $c^{\alpha}(\boldsymbol{\mu}, T) = -\partial\psi_{\text{bulk}}^{\alpha}(\boldsymbol{\mu}, T)/\partial\boldsymbol{\mu}$ (Choudhury & Nestler, 2012). Besides the mass conservation $\nabla \cdot \boldsymbol{u} = 0$ the momentum balance is solved, which is given by

$$\frac{\partial\boldsymbol{u}}{\partial t} + (\boldsymbol{u} \cdot \nabla)\boldsymbol{u} + \frac{1}{\rho}\nabla p = \nu\Delta\boldsymbol{u}. \tag{8}$$

Therein, the pressure gradient is denoted by ∇p and the Laplace operator by Δ. The kinematic viscosity of the fluid is given by ν and the mass density of the fluid by ρ. Note: In general (e.g., multi-phase flow problems (Reder et al., 2022)), the phase-specific material parameters are interpolated in the diffuse interface regions. In this study we focus on single phase flow and therefore the corresponding parameters in Table 1 are utilized. The fluid velocity $\boldsymbol{u}$ is computed by the volumetric average of the present phases and is given with $\boldsymbol{u} = \sum_{\alpha=1}^{N} \phi_\alpha \boldsymbol{u}_\alpha = \phi_l \boldsymbol{u}_l$. Therefore, the adapted mass and momentum conservation equation within the phase-field context read as

$\partial(\phi_l \boldsymbol{u}_l)/\partial t + (\phi_l \boldsymbol{u}_l \cdot \nabla)\phi_l \boldsymbol{u}_l + \phi_l/\rho \nabla p = \nu \Delta(\phi_l \boldsymbol{u}_l) - \mathbf{M}_l^d$ and $\nabla \cdot (\phi_l \boldsymbol{u}_l) = 0$. Therein, $\mathbf{M}_l^d = \chi \nu \phi_s \boldsymbol{u}_l/\epsilon |\nabla \phi_l|$ is a dissipative interfacial stress term (see Beckermann et al. (1999)), where χ is a dimensionless parameter which controls the fluid velocity in the diffuse interface and is chosen for the multi-obstacle potential as $\chi = 7.989$. In a pure liquid region, the term vanishes and also ensures that the fluid velocity at the grain-liquid interface is zero (no-slip). The Navier-Stokes equations are only solved where a liquid phase is partly or fully present since the solid grains are assumed to be impermeable. From the numerical point of view, the solver checks at each time step each cell if a liquid phase is present and a flag for the fluid flow computations is activated in the corresponding cells. After the fluid flow is computed, the concentration equation is evaluated with the updated flow velocities. Finally, the phase fields are updated with the corresponding driving forces from the supersaturated fluid. Therefore, the presence of the liquid phase is determined by the evolution of the phase fields and due this diffuse interface approach no explicit interface tracking or remeshing of the liquid region is necessary.

2.3. Computational Treatment With Assumptions

The above discussed model equations are implemented in the in-house solver Parallel Algorithms for Crystal Evolution in 3D. We refer interested readers to Hötzer et al. (2018), where a detailed description of the utilized optimization and parallelization algorithms is given.

In order to reduce computational costs for the numerical modeling of crystal growth in multi-grain structures we perform all simulations exclusively in 2D. However, the numerical solution scheme and implementation are realized in 3D with the presented phase-field model, although the computational time increases drastically.

Here, the effects of the concentration dependent crystal growth are investigated in a flow channel with potash alum ($KAl(SO_4)_2 \cdot 12H_2O$). This mineral is chosen since the length scale in which the supersaturation changes (and the resulting effects are visible) is comparatively small and can be resolved in reasonable computational time (Note: For e.g., quartz the length and time scale are orders higher). Crystal growth experiments with potash alum in a flow channel have been performed in previous studies (Hilgers & Urai, 2002; Hilgers et al., 2004; Nollet et al., 2006). System parameters for example, Péclet number, saturation state, are used in the present work and are given in Table 1. Further quantities are extracted from other literature and also given in Table 1. We remark that the same conditions as the flow through experiments of Hilgers and Urai (2002) (e.g., temperature, Reynolds/Péclet number) are chosen for the phase-field simulations to ensure a direct comparability with the corresponding laboratory experiments. However, the chosen conditions are not a limitation of the modeling approach and simulation studies can be extended to other chemical conditions (p, c, T) and minerals in future works to mimic conditions in subsurface environments.

For the crystal shape of potash alum, we use the shape described in Nollet et al. (2006) (their Figure 4b) and rotate the 3D shape as depicted in Figures 1a and 1b such that a 2D projection with {110} and {111} facets is obtained. We note that other crystal habits which potash alum can attain could be easily incorporated (e.g., additional facets) by adapting for example, the mobility coefficient. However, we limit our investigations to this particular crystal shape for the sake of simplicity.

In general, the grand potential energy functional can be dependent on the temperature. We assume that the temperature conditions in the flow channel are isothermal and therefore set the temperature to constant and do not compute a temperature equation explicitly. The temperature determines the equilibrium concentrations in the system, which are consequently also constant.

3. Results

3.1. Single Crystal in Supersaturated Fluid

In this section, we computationally analyze the precipitation of a single potash alum crystal inserted in a supersaturated liquid phase by employing the proposed modeling and simulation approach. The initial setup for the crystal with the concentration field is depicted in Figure 2a. At the upper edge a Dirichlet boundary condition is applied where the supersaturation given in Table 1 is prescribed. This results in a diffusive influx in the liquid phase, which is depleted by the crystal growth and has a lower saturation state. We investigate the crystal growth in two different cases, whereas in the first case the diffusion is fast and in the second case the diffusive mass transport is slow compared to the attachment kinetics. Therefore, we use the parameters from Table 1, whereas the

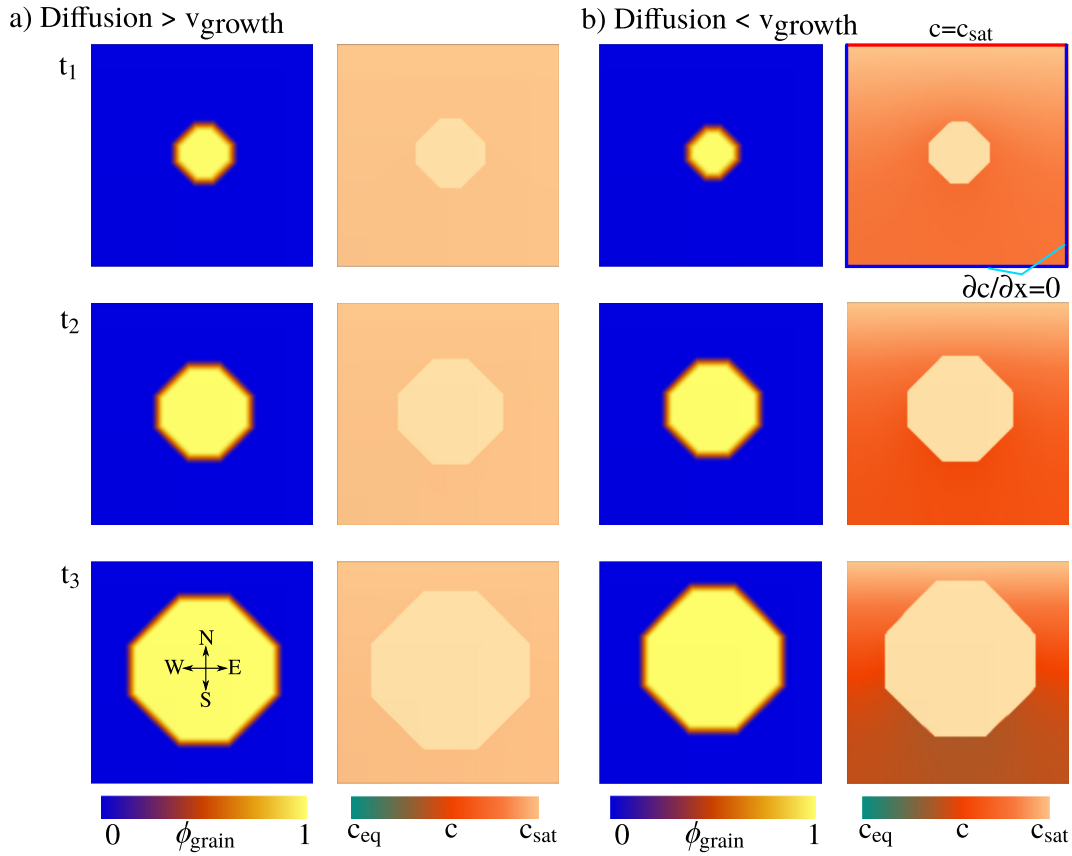

Figure 2. Single potash alum crystal in a supersaturated fluid. Diffusion of supersaturated fluid is (a) faster and (b) slower than the attachment kinetics. The phase-field and concentration field are depicted on the right and left side, respectively. The crystal growth rates are plotted in Figure 3 in the directions marked in panel (a) at t_3.

mobility for the first case is set to $M^I_{s,l} = 0.01 \times M_{al.\text{-}liq.}$ and for the second case to $M^{II}_{s,l} = M_{al.\text{-}liq.}$. We chose the bulk free energy density in Equation 5 to $f^\alpha(c^\alpha(\boldsymbol{\mu})) = A\left(c^\alpha(\boldsymbol{\mu}) - c^\alpha_{\text{eq.}}\right)^2$ with a quadratic shape (similar as in Mai et al. (2016)) and set the calibration parameter for free energy to $A = 265$ J m^{-3} in all simulations. We calibrated the mobility in the second case to obtain the averaged growth rate of potash alum of $v_{gr.} = 2.6 \times 10^{-5}$ mm/s, which is similar as measured in Hilgers and Urai (2002) and Nollet et al. (2006). With the chosen mobilities the effects of dominant mass diffusion or surface reaction on the crystal growth can be observed.

In the first case diffusive mass transport from the inlet into the domain occurs (chemical potential), however, since the attachment kinetics is slower compared to the diffusivity a nearly homogeneous concentration field

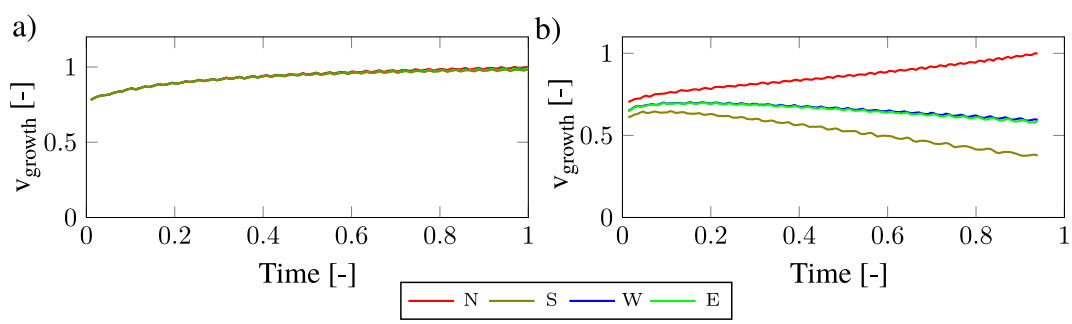

Figure 3. Crystal growth rates from Figure 2 in North (N), South (S), East (E), and West (W) direction for the cases where diffusion is (a) slow and (b) fast compared to the attachment kinetics. The time is normalized to the total simulation time and crystal growth rate to the maximal occurring value.

surrounds the crystal (Figure 2a). Therefore, the crystal grows due to the nearly homogeneous supersaturation in all direction with nearly the same velocity (Figure 3a). Over time, the crystal size increases and therefore also the growth rate slightly increases, since more surface is accessible for the attachment reaction.

In the second case, the attachment kinetics compared to the diffusive mass transport is increased by utilizing a higher mobility $M_{s,l}^{II}$. This choice results in a visible local depletion of the supersaturated fluid and in turn causes different crystal growth rates in the different directions (Figure 2b). Therefore, the crystal shape evolves slightly distorted compared to its equilibrium shape. Additionally, the crystal becomes wider in horizontal direction over time, which reduces the space of the liquid phase, in which diffusive mass transport occurs. This further reduces the growth rate of the bottom face during later stages of the crystallization (Figure 3b). In this setup, we measure a reaction rate coefficient of $k = 0.00656\ \mathrm{s}^{-1}$.

3.2. Polycrystalline Growth With Pure Diffusion

In the next step of complexity, we extend the single crystal setup from the previous section to a multi-grain system. The utilized parameters are the same as given in Table 1, whereas the mobility is chosen as in the example in Figure 2b and reproduces crystal growth rates for potash alum from laboratory experiments. This choice implies that the attachment kinetics for potash alum is faster than the diffusive mass transport (see Figure 2b). The initial simulation setup for the phase-field and concentration field is depicted in Figure 4a. We insert 16 randomly oriented grains at the lower edge of the domain, whereas on the upper edge a constant supersaturation (as in the previous example) is imposed. Similarly, as in the previous case, diffusive mass transport occurs into the direction of the crystals since the crystal growth depleted the concentration field locally.

In natural systems crystal growth rates can be hetero- or homogeneous depending on the environmental conditions, crystal surface state (euhedral vs. anhedral), presence of crystal defects or coatings on crystal surfaces. Here, we focus on the effects which can be attributed to (I) partially coated crystal surfaces or (II) induced dislocations. From an experimental point of view, the first case could be caused due to a grease film from the fingertips of the experimental preparator and the second case could be caused by crushing the potash alum crystals in the mortar before the crystal growth experiment and thereby inducing crystal defects into the crystal lattice.

In order to test the effects of different crystal growth behaviors on the evolving microstructure, we investigate three cases of crystal growth. In the first case we assume that no crystal growth rate difference occurs and set the mobilities of all crystals homogeneously to the same constant value ($M_{s,l} = M_{al.\text{-}liq.}$). Note: The mobility appears in the modeling approach in Equation 6 as a relaxation parameter and controls the crystal growth rate. To incorporate the effects of different growth rates, we test two additional cases where the mobilities for crystal growth are set as a two-class system or are randomly assigned within a value range. We model the different growth rates with a decrease of the interface mobility of alum grains to the liquid phase by distinct value which remains constant in each phase over time. In the two-class case, the growth rate of some grains is reduced with a unified ratio (similar as in Spruženiece et al. (2020)), which results in both fast and slow growing crystals. This choice implies that only some grains are either coated and/or induced by dislocations. In the randomly distributed case, each grain is assigned with a unique random mobility, which mimics the behavior of different strongly coated surfaces and/or a different amount of induced dislocations.

In the homogeneous constant case the crystals start to grow into the supersaturated fluid. The crystals have different crystallographic orientations, which is resulting in growth competition and termination of unfavorably oriented crystals. We observe a homogeneous growth front, which is attributed to the crystallographic anisotropy of potash alum, where the preferential directions are not as strong as for example, in quartz. However, the evolving crystal structure does not resemble the laboratory crystal growth experiments of Hilgers and Urai (2002), Hilgers et al. (2004), and Nollet et al. (2006), where a heterogeneous growth front and a wide range of crystal sizes are observed (see Figure 8a). In this setup the Damköhler number is $\mathrm{Da}_{\mathrm{II}} = 10.3$, whereas we set the crystal surface in contact with the liquid phase as characteristic length.

In the two-class case the fast-growing grains out-compete the slow-growing grains shortly after the simulation started and expand over them close to the rim. This results in the presence of only fast-growing grains at later stages of crystal growth. In the early stages of growth, the velocity is heterogeneous causing a rough overall front profile, while at a later stage, fast-growing crystals form grain boundaries and a homogeneous smooth front with larger grain sizes is established. In intermediate stages, we observe some regions between fast-growing grains, where a liquid gap occurs between neighboring fast-growing grains (on right in Figure 4c) in which the crystal

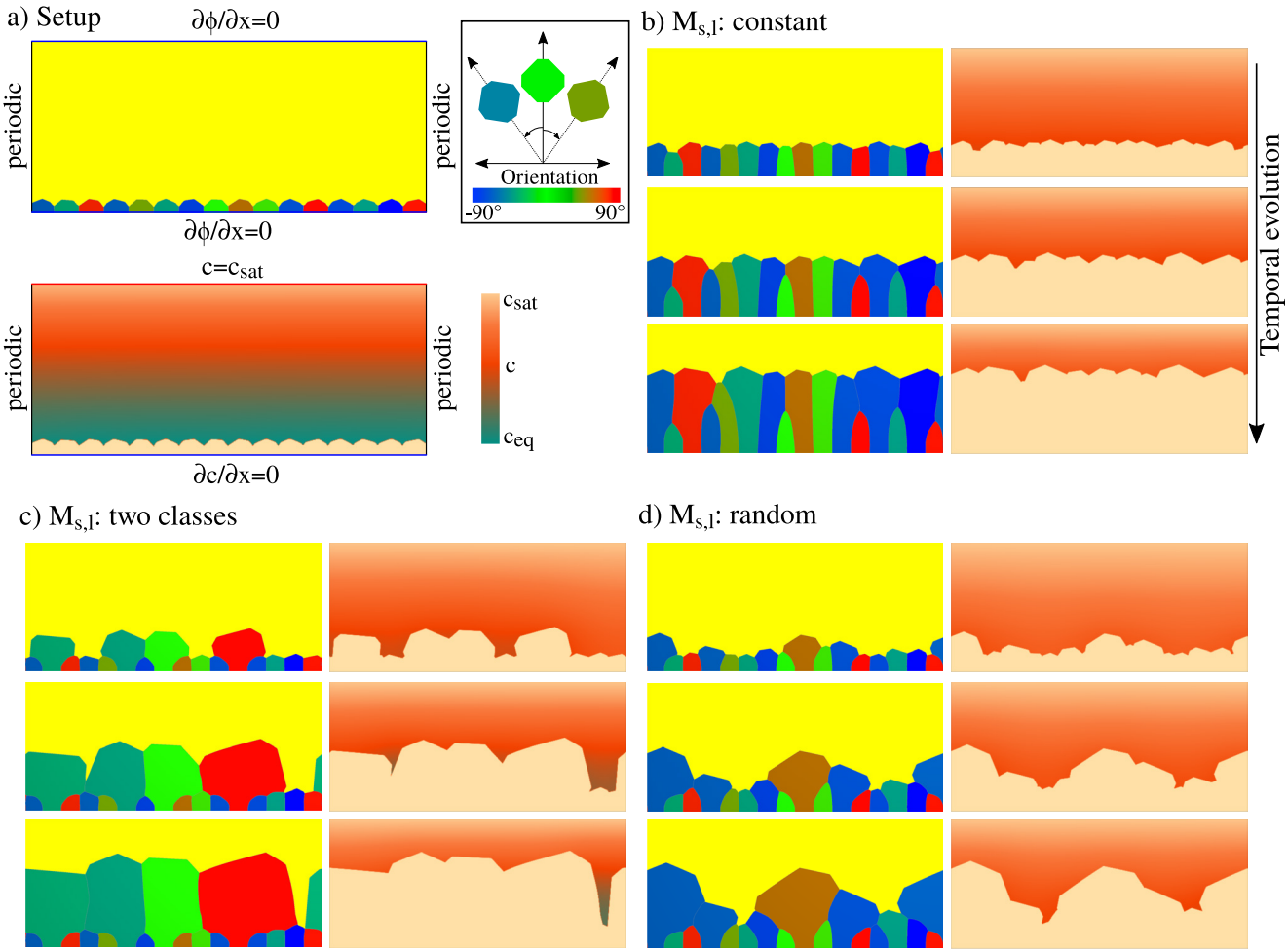

Figure 4. Multi-grain setup with pure diffusive mass transport. (a) Initial setup of the phase-field and the respective concentration field with boundary conditions. The color of the potash alum grains illustrate their crystallographic orientation. A constant supersaturation is applied on the upper boundary. (b–d) Temporal evolution of the crystal structure at three representative time steps. The phase-field is in the upper and the concentration field in the lower column. In (b) the mobility $M_{s,l} = M_{al.\text{-}liq.}$ is chosen to be equal for all crystals, in panel (c) two classes for the mobilities (fast: $M^f_{s,l} = M_{al.\text{-}liq.}$ and slow: $M^s_{s,l} = 0.2 \times M_{al.\text{-}liq.}$) are applied and in panel (c) each grain is assigned a random mobility: $M_{s,l} \in (0.172, 1) \times M_{al.\text{-}liq.}$.

growth is slower than at the upper growth front (due to local depletion). The overall growth rate is similar to the homogeneous case, however, the Damköhler number $Da_{II} = 15.01$ is higher due to the larger surface area. The displayed crystal structure at intermediate growth stages corresponds better to laboratory experiments as presented in Hilgers and Urai (2002), Hilgers et al. (2004), and Nollet et al. (2006) (see Figure 8a). However, in later stages when a homogeneous growth front and similar sized crystals are present the grain structure of the simulations differs from the laboratory experiments.

In the randomly distributed case all potash alum crystals grow with a different rate. This leads to a rough heterogeneous growth front with a surface area between the previous two cases and heterogeneous crystal size distribution during all stages of crystal growth. The microstructure with few large crystals resembles the respective experiments including fluid flow during all stages of crystal growth (see Figure 8a). This advocates that the crystals in the laboratory experiments might have observed a growth rate anisotropy. The Damköhler number is $Da_{II} = 12.55$, which is as expected in between the former two cases.

3.3. Polycrystalline Growth With Lateral Flow

In this section we investigate the crystal growth in a flow channel, where the concentration field is additionally advected by a fluid velocity. Based on the observations in the previous section, we analyze two different cases

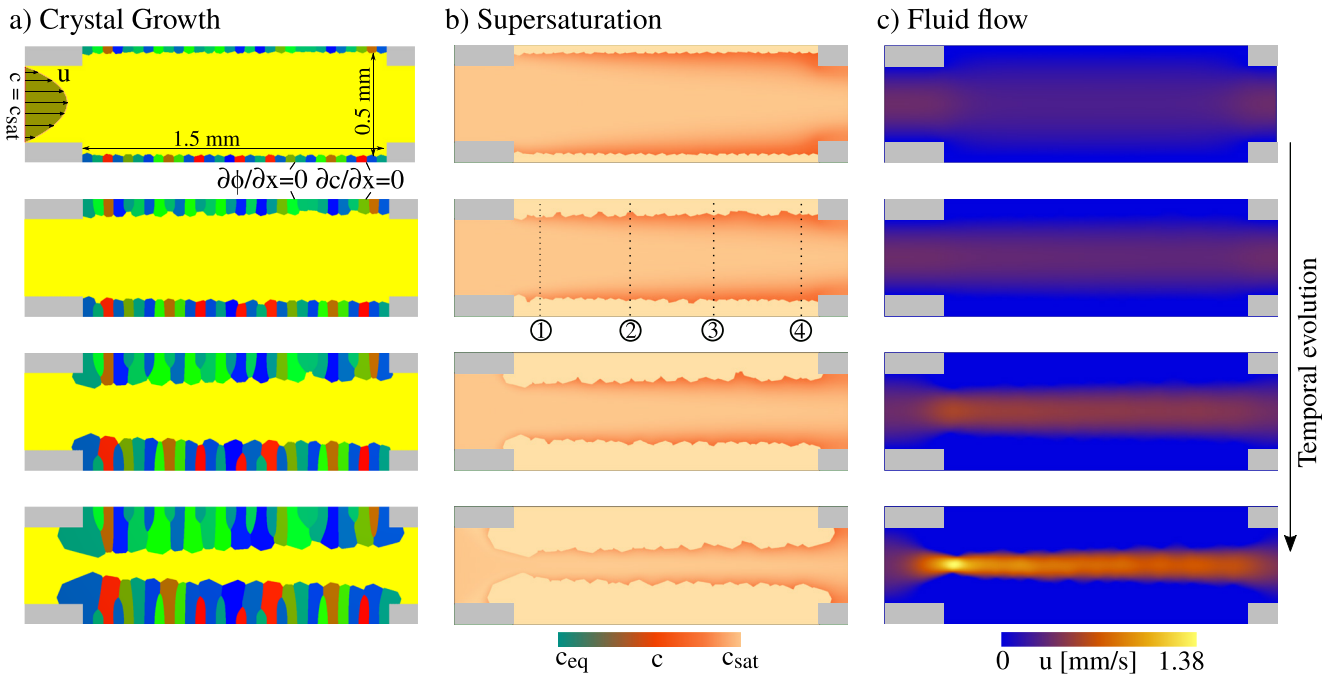

Figure 5. (a) Setup of flow channel with potash alum grains at upper and lower boundary (color indicates orientation; see Figure 4a). The applied boundary conditions (for fluid flow, phase-field, and concentration) are depicted. A zero-pressure boundary condition at the right side is applied for the fluid flow. Temporal evolution of (a) crystal structure, (b) concentration, and (c) fluid flow. The open fracture seals over time, whereas the crystal at the inlet grow faster than the crystals at the exit. The concentration of the supersaturated fluid is denoted by c_{sat} is the and the equilibrium concentration by c_{eq}.

of flow-through experiments. In the first case the effects of different supersaturations and flow velocities on the evolving microstructure are investigated and quantitatively compared to laboratory experiments. To elaborate these effects independently of the crystal growth rate (which might vary due to crystal defects or coatings; see Figures 4b and 4c) we utilize the same mobility for all grains similar as in Figure 4a. In the second case we modify the individual crystal growth rate randomly as in Figure 4c to mimic the crystallization in a more representative crystal structure. We use the parameters from Table 1 unless stated otherwise.

The setup and prescribed boundary conditions for the first case related to equal growth dynamics of the crystals are depicted in Figure 5a. We mimic the flow channel of the laboratory experiments of Hilgers et al. (2004). Their chosen setup and parameters (e.g., supersaturation, fluid velocity) result in a measurable growth rate difference along the relatively short flow channel and enable a coupled microstructural simulation of the grain growth in a flow channel in reasonable computational time. In Figure 5 the gray areas indicate the stationary inlet and outlet of the channel, where no evolution equations are computed. This ensures that the flow profile of the supersaturated fluid can be directly assigned and is not affected by growing crystals directly at the inlet. We insert 30 potash alum grains at the upper and lower edge, which are randomly oriented. At the lower boundary the crystal orientation is repeated after the first 16 grains to better visualize the impact of a depleted supersaturated fluid on the crystallization over the length of the fluid channel. The crystals grow into the fluid (Figure 5a) due to the (locally different) present supersaturation (Figure 5b). The growth of the crystals depletes the local concentration field, which is then advected by the present fluid flow velocity and results in a decreasing supersaturation along the flow channel. The profiles of the supersaturation are evaluated (after 34 min) across the vertical lines 1–4 marked in Figure 5b and plotted in Figure 6b. This causes a faster crystal growth rate near the inlet and a decreasing crystal growth along the channel, whereas the crystallization is the slowest near the outlet. Moreover, the fluid flow velocity increases (Figure 5c) while the crystals from both channel walls grow together and continuously narrow the remaining channel, since a constant flow rate is applied as in the experiments. The maximum fluid velocity is extracted as a function of time in Figure 6a.

Additionally, the effect of different supersaturations ($S = 1.09$ and $S = 1.14$) and flow velocities ($u = 0.08$ and $u = 0.16$ mm/s) is investigated with this setup. When a higher flow velocity is chosen (twice as high as before) the overall crystal growth rate increases compared to the previous case (Figures 6c and 6d), because more potash

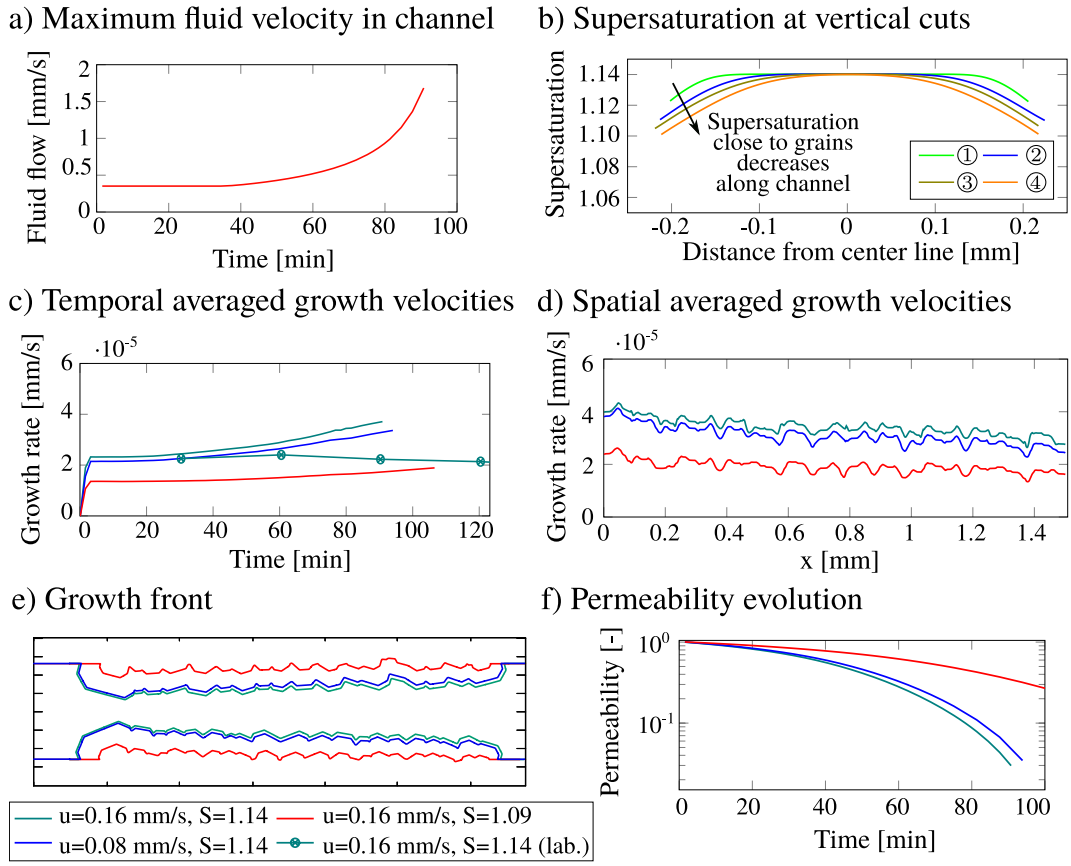

Figure 6. Analysis of simulations from Figure 5. (a) Maximum flow velocity in stream direction increases over time. (b) Present supersaturation at different positions in Figure 5b. Supersaturation at grains is higher at inlet than at outlet and decreases along the channel. (c) Temporal and (d) spatial averaged crystal growth rate compared to experiments from Hilgers and Urai (2002) (see also Figure 8a). (e) Growth front at same time for different supersaturations and flow velocities. (f) Semilogarithmic plot of permeability evolution over time for the three cases. The permeability is normalized to the initial value of the open channel. Legend in bottom row refers to panels (c–f).

alum (in the solution) provided by the Dirichlet boundary condition at the left side of the domain streams into the channel and the ratio between attachment kinetics and mass transport decreases. Furthermore, the growth front becomes slightly more homogeneous since less difference in the supersaturation is present along the channel (Figure 6e) and the permeability in the flow channel decreases over time more slowly (Figure 6f). Note: The temporal permeability evolution shows a similar trend as the compact quartz case in Kling et al. (2017). In contrast, when a lower supersaturation is chosen, the potash alum crystals grow slower (lower crystallization driving force). The roughness of the growth front, the temporal and the spatial growth rate show a more homogeneous behavior. Due to the identical mobility of all crystals, a non-negligible deviation of the simulated microstructure from the experiment (Hilgers & Urai, 2002) can be recognized.

Furthermore, we observe a difference of the trends (of the plots) between the numerical and the experimental growth rate in the measurements of the temporal averaged crystal growth rate (Figure 6c). In the simulations the growth rate increases over time, while, in the experiment, the rate is almost constant ($v_{exp.} \approx 2$ mm/s). As the crystals grow, the fluid channel narrows. This increases the velocity in the remaining fluid and the concentration-rich fluid flows with almost c_{sat} to the growth front. This in turn increases the concentration gradient and the driving force for growth.

In the second case, a growth rate difference between the crystals is applied as in Figure 4c, where each crystal has a unique random mobility (Figure 7). We insert a randomly oriented grain package at the upper and lower boundary (Figure 7a), mimicking the initial structure of the flow experiment of Hilgers and Urai (2002). Since the grains are assumed to have different growth rate, the growth competition is stronger than before and slower grains are out-competed close to the rim, whereas faster crystals expand over them and become wider than in the previous case (Figure 5). Similar as before, the local concentration depletes due to the crystal growth, which

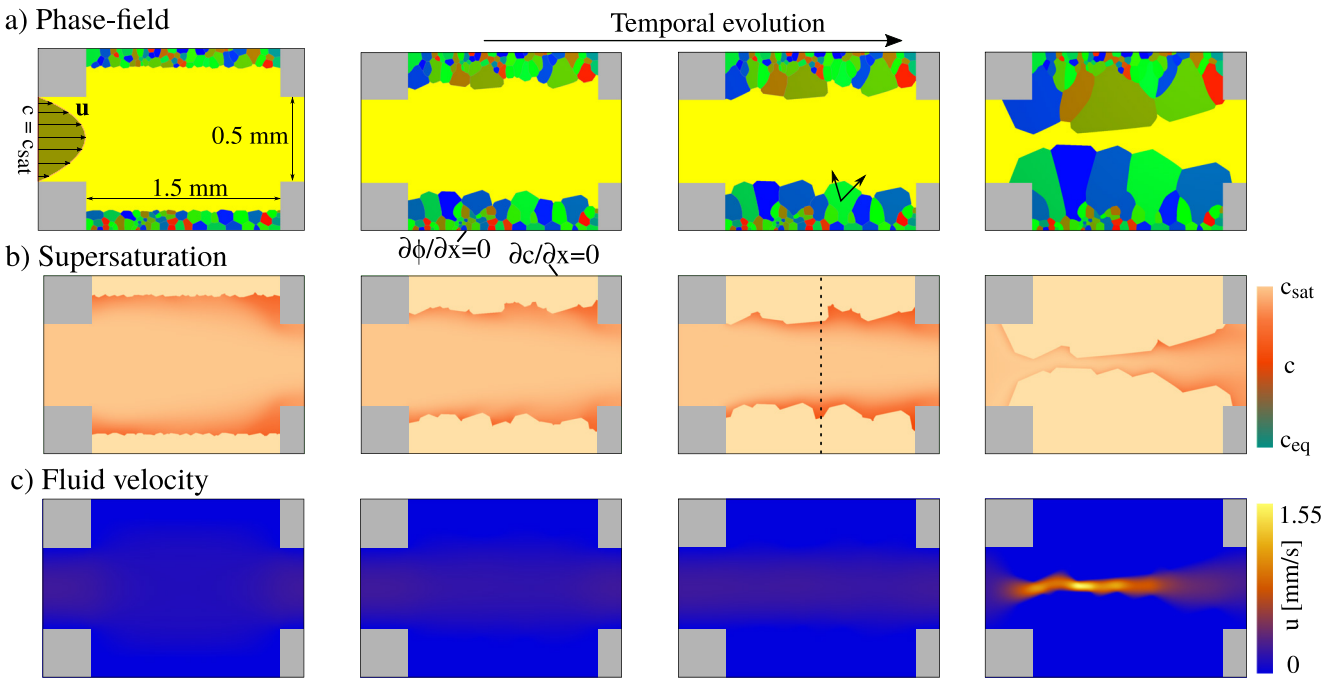

Figure 7. (a) Setup of flow channel with alum grains at upper and lower boundary (color indicates orientation; see Figure 4a) with the applied boundary conditions (for fluid flow, phase field, and concentration) on left. Temporal evolution of (a) crystal structure, (b) supersaturation, and (c) fluid velocity are depicted from left to right. The open fracture seals over time, whereas the crystals at the inlet grow faster than the crystals at the outlet.

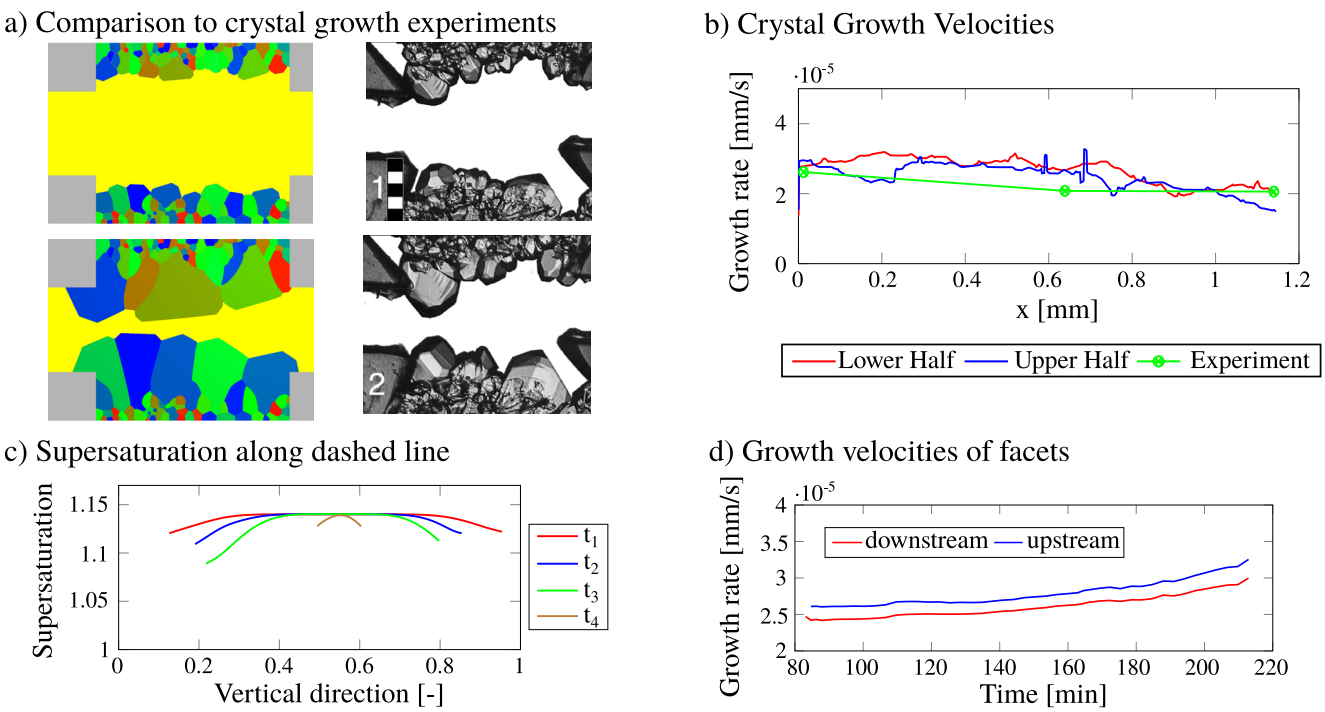

Figure 8. (a) Comparison of phase-field results to laboratory growth experiments from Hilgers and Urai (2002) of potash alum growth in a flow channel. Reprinted with permission from Hilgers and Urai (2002). (b) Spatial crystal growth rate compared to these experiments. (c) Supersaturation along dashed line in Figure 7b at different times (left to right in Figure 7). (d) Crystal growth rate of two facets of green crystal in Figure 7a facing in upstream and downstream direction. Growth rate is slower for downstream facet.

leads to a decreasing supersaturation along the flow channel (Figure 7b) and larger crystals at the channel inlet. Furthermore, due to the rougher growth front compared with the previous case the fluid flow field becomes more inhomogeneous and tortuous during the crystal growth due to the evolving crystals (Figure 7c). The resulting microstructure (Figure 8a) exhibits a convincing agreement with the grain structure observed in the laboratory experiments from Hilgers and Urai (2002).

Additionally, we calculate the crystal growth rate of the grains on the upper and lower halves along the flow channel. The crystallization rate shows a similar trend than in the previous case (Figure 8b) and agrees with the crystal growth experiments of Hilgers and Urai (2002). Note: Similar to Figure 6c, we also observe here a deviation of the trend of the temporal averaged growth rates compared to the laboratory experiments.

Moreover, the temporal evolution of the supersaturation along the dashed line in Figure 7b is depicted in Figure 8c. Since crystals which are located in upstream direction deplete the supersaturation and partially block the fluid flow, the supersaturation decreases over time. Additionally, we measure the growth rate of two different facets of the green crystal (marked in Figure 7a), where one facet shows in upstream direction and the other facet is directed downstream. The upstream facet grows at a higher rate than the downstream facet (similarly as in Nollet et al. (2006)), since the upstream facet deflects the supersaturated fluid flow and the impact of the advective mass transport is lower than at the upstream facet (Figure 8d).

4. Discussion

The presented studies demonstrate the capability of the phase-field method to quantitatively describe crystal growth in domains where advective and diffusive mass transport is present. With the help of this modeling approach, experiment results (e.g., Hilgers & Urai, 2002) can be recreated while additionally quantities and coupled physical mechanisms can be described which cannot be easily resolved by laboratory experiments. The models enable new insights into microstructure formation under the influence of diffusion and advection and can therefore improve the understanding of the crystallization process by locally resolving fluid related quantities (e.g., supersaturation, fluid flow velocity in channel and its variability due to the shape of the growing crystals).

We chose this particular setup to enable a direct comparability to existing laboratory experiments and also show the applicability of the phase-field method to reactive flow and its interaction with a heterogeneous polycrystalline wall rock structure. The results can support field experiments by giving insights to the hydrological behavior of single fractures and its response due to THMC processes on small length scales and can then be up-scaled to simulations on larger length scales. This can be achieved for example, by calculating the effective growth properties on microscale and apply these rates and characteristics in simulations to study the behavior at larger time and length scale (e.g., Hilgers et al., 2004). The phase-field method is used here since it allows the modeling of polycrystalline systems with phase-specific parameters, whereas anisotropy formulations enable the depiction of faceted growth kinetics. Additionally, the coupling of phase evolution with reactive fluid flow is possible and allows to describe crystal growth without an explicit remeshing technique. The presented phase-field framework uses a grand-chemical potential approach where phase changes appear when chemical potential is in non-equilibrium and it is easily possible to extend the present studies with the incorporation of thermodynamic data obtained from phase diagrams and apply the precipitation of different minerals simultaneously due to multiple components. Furthermore, the phase-field framework enables to directly include effects of solid phase transport in multiphase-flow (e.g., detached particles clog fluid pathways; see Reder et al. (2021)), or effects of mechanical fields can be included (e.g., crack formation: Prajapati, Herrmann, et al. (2020)). Additionally, the phase-field approach and achieved simulation results show good agreement with natural crystal structures (e.g., quartz, calcite, cf. Ankit et al., 2015; Spruženiece et al., 2021) and the presented results show qualitative agreement to laboratory flow through experiments. This advocates the utilization of the phase-field method for describing reactive flow with precipitation. As the phase-field technique can include coupled physical processes and be extended to different mineral species, it is considered to enhance the modeling capabilities in subsurface systems. It is especially suited to assess contaminated groundwater interacting with the subsurface, water production, wastewater storage, and geothermal applications.

The results in the presented system can improve the understanding of fracture sealing and the controlling factors of supersaturation and fluid flow velocity in natural environments. As the crystal growth rate is a function of the local flow velocity and supersaturation, a heterogeneous growth front can be established.

For natural environments, the generalized outcomes are:

- A low flow velocity in combination with fast reaction kinetics will result in a heterogeneous growth front (e.g., leading to localized blockage).
- Surface coatings or crystal defects of the host rock will result in a heterogeneous flow path.
- Crystal heterogeneity may record preferred fluid flow directions in incompletely sealed fractures.
- Regions cut off from advective fluid transport, will record slower growth rates, and will subsequently alter the mechanical properties of the whole system (e.g., Späth et al., 2022b).

4.1. Agreement and Differences With Laboratory Results

In the presented work, we do not observe fluid inclusion as commonly noticed in natural vein microstructures or as in crystal growth experiments (Nollet et al., 2006). This could be attributed to either a high supersaturation along the (comparatively small) flow channel, only modeling crystal growth (no alternating crack-sealing (Ramsay, 1980)), or a general limitation of the applied models. In future works this effect could be incorporated and applied for example, to investigate the effects of multiple fracturing events while using a concentration dependent driving force.

We apply two different supersaturations in the fluid phase (S = 1.09 and 1.14) and two flow velocities (Pe = 80 and 160) in this work, which show a visible and quantitative agreement to laboratory experiments. The utilized parameters indicate a dominance of advective to diffusive mass transport and can explain a decreasing growth rate along the channel. These supersaturations cause only precipitation on wall rock crystals, whereas no nucleation of crystals in the fluid is observed, since the supersaturation is below the metastable region, where nucleation might occur (Barrett & Glennon, 2002). However, at higher supersaturations, a direct nucleation of a crystal in the fluid is expected to occur, which could also cause clogging of natural and experimental fractures. This effect of crystal nucleation is not incorporated in our modeling approach so far and could be addressed in future works discussing higher concentrations. In order to include the effect of crystal nucleation the presented phase-field model could be adapted with a nucleation mechanism. For example, parts of the work of Schoof et al. (2018) on phase nucleation could be extended with a criterion where nucleation is dependent on the present supersaturation and chemical composition of the fluid and is activated once the metastable region is reached.

In the experimental works of Hilgers and Urai (2002) and Hilgers et al. (2004) the formation of isolated long crystals into the fluid was observed at some positions in the flow channel, whereas in our simulations the growth front is more homogeneous. This could be attributed to the choice and (low) range of the assigned mobilities in our studies (see Figures 4 and 7). In the laboratory experiments the range could be larger due to either more present defects in the crystal lattices, a higher variability of crystal surface coatings, or a larger substrate size on which precipitation occurs, as larger substrate sizes correlate positively with the size of precipitating crystals (Busch et al., 2021; Lander et al., 2008). The presented approach of assigning phase-specific mobilities could be extended in future works by adapting the mobility of certain crystal facets which show defects or by resolving a surface coating with an additional inert phase between grain and liquid.

In the presented work, crystal growth is slower at the channel outlet compared to the inlet, as the solute concentration is continuously reduced due to precipitation and the supersaturation is therefore lower. This is also observed in laboratory flow through experiments (e.g., Busch et al., 2021; Hilgers et al., 2004), where precipitates located closer toward the flow inlet are larger and contain more mass. However, experimental setups can also show different trends in the crystal size distribution, where precipitates are distributed uniformly, randomly or concentrated near the inlet or outlet. This heterogeneity in crystal sizes along the flow path can be attributed to the substrate size of the particles, on which the syntaxial precipitation occurs and may be another controlling factor to explain mixed results obtained in experimental flow through setups, as it is seldomly quantified. Larger substrate sizes result in larger crystal sizes of the precipitated material. A small substrate size located close to the inlet may likely form precipitates which are smaller than those formed on larger substrates further downstream (Busch et al. (2021), their Figure 13). The presented phase-field simulations allow to control these parameters explicitly and the rate of precipitated volume in relation to substrate size (grain size) is inherently included in the simulation workflow. In this work the substrate size is similar for all alum grains, to only highlight the effect of concentration changes along the flow path, and to present the generalized effect of these changes on mineral precipitation. Alternatively, the physico-chemical conditions (p, c, T) in experimental setups may not be as consistent

as assumed from the selective measurements at certain points along the flow path, which may again alter the precipitation rates and affect the solute concentration and therefore might also cause nucleation.

4.2. Limitations and Assumptions of the Model

The presented numerical studies are performed solely in 2D in order to limit computational costs for the coupled calculation of the phase-field equations, the concentration field, and the incompressible Navier-Stokes equations in the polycrystalline structures. Nevertheless, the model equations are formulated such that they are directly applicable in 3D, but an increase of computational costs arises. Even though the 2D simulations show a sound agreement with the laboratory experiments of Hilgers and Urai (2002), an application of the methods to 3D would enable a more heterogeneous crystallographic orientation (in-plane rotation vs. full 3D rotation) and an incorporation of the third (out of plane) growth direction. Therefore, the 2D simulations are missing the additional growth competition with crystals from outside of the simulation domain. Additionally, once the crystals grow together into the channel center the flow is deflected from the largest crystals and the fluid connectivity is reduced. After two crystals touch in our simulative approach the crystal growth behind this touching point stops since the fluid flow is completely blocked, even though there still might be fluid connectivity in a 3D setup (similar as in laboratory experiments). Therefore, an extension to 3D seems reasonable to predict the crystal growth and permeability evolution in natural environments. Previous phase-field studies of crystal growth in 3D (e.g., Ankit et al., 2015; Spruženiece et al., 2021; Wendler et al., 2016) showed a visible good agreement with 2D simulations (see e.g., Figure 13d in Späth et al. (2021)). We expect that the obtained 2D results would not change fundamentally when extending the domain into 3D as long as the flow channel is not blocked.

Our modeling approach demonstrates promising results with potash alum and agrees with experimental data, however, we note that this approach seems to be mostly applicable in cases where the solubility of the present mineral is high (here 15.35 g/100 g H_2O) and a comparatively high supersaturation is present (here $S = 1.14$). This leads to a significant depletion of the supersaturated fluid and a decrease of the driving force at the grain scale over a few millimeters. However, for minerals which frequently occur in nature (e.g., quartz) and for which the solubility is lower (e.g., ≈100 ppm (Okamoto et al., 2010) for quartz), the length scale of significant depletion and the decrease of supersaturation is occurring over a larger distance (e.g., Lee & Morse, 1999). Therefore, it still seems reasonable to utilize the assumption of *constant supersaturation* for these minerals at mesoscopic length scale (µm range). However, once computational resources improve and larger domains with a fully resolved grain structure can be computed the presented model could also be applied to minerals as quartz and then be utilized to predict larger length scales.

4.3. Incorporation of Additional Effects into Crystal Growth Modeling

With the utilized modeling approach the effects of a depleting concentration along the flow channel can be described. Since the locally present supersaturation depletes during crystal growth and is advected the crystal growth rate decreases along the flow channel and depends on the prescribed fluid flow velocity and supersaturation. However, previous studies (Colombani, 2008; Herman & White, 1985; Liu & Dreybrod, 1997; Opdyke et al., 1987) discuss the effect of a fluid flow velocity on the crystal evolution based on the thickness of a diffusional boundary layer, whereas a thicker diffusional boundary layer occurs when fluid flow is slow and becomes thinner with higher flow velocities and results in a slower and faster crystal evolution respectively. This additional effect is to be incorporated in future studies by adapting the mobility to a dependency regarding the local fluid flow velocity.

In this work we focus on the evolution of crystals in a supersaturated fluid on the grain scale. This gives insights into the temporal and spatial development of the crystalline microstructure, while also visualizing the local distribution of supersaturation and fluid velocity. Even though we did not explicitly investigate the effects of crystal growth on larger length scales (e.g., reservoir scale), the present simulative approach can be used in combination with upscaling techniques to understand the behavior of fractured or porous rocks on macroscopic length scales over geologic time scales.

5. Concluding Remarks

This work presents the modeling of supersaturation dependent driven crystallization in open fractures, where the phase-field evolution equation is coupled with a concentration equation and the Navier-Stokes equations.

The presented work highlights the versatility and capability of the multiphase-field method in modeling crystal growth in open fractures or flow channels, whereas the results show a sound agreement to laboratory experiments of Hilgers and Urai (2002), Hilgers et al. (2004), and Nollet et al. (2006). This approach enables the depiction of different crystal growth rates depending on the local supersaturation state and possible crystal defects or crystal surface coatings.

Our studies include that the crystal growth rate depends on the local supersaturation state, which in turn is controlled by the ratio of advective and diffusive mass transport to the attachment kinetics. The crystal growth rate decreases along the flow direction due to fluid depletion. A higher mass transport compared to the attachment kinetics results in a more homogeneous supersaturation and similar crystal growth rates, whereas inhomogeneous crystal growth rates occur when the mass transport is slower (Figure 2). In addition, the crystal growth rate and thus the resulting microstructure may depend on induced crystal defects or coatings on the crystal surfaces.

In future works the findings of this study can be extended into 3D to enable a fluid flow around crystals in all directions avoiding a blocking of the flow channel once crystals have touched. Moreover, an extension to larger domains with minerals frequently occurring in nature (e.g., quartz) in possible combination with multi-crack-sealing (e.g., Späth et al., 2022a) and a potential collapse of the fracture (due to pressure loss). Additionally, the present modeling approach could also be used for upscaling the microstructural findings to reservoir length scales. This can help to gain a better understanding of the formation of vein microstructures in subsurface environments and to discover unknown physical mechanisms in geothermal reservoirs or subsurface environments. Furthermore, the current approach of using a concentration field for the driving force of faceted crystal growth can be extended to incorporate additional subsurface processes in the modeling approach, such as pressure solution creep (Guével et al., 2020) or corrosion. Therefore, existing phase-field models which include mechanical effects into the phase evolution could be adapted to the presented work at microscale level and the outcome of those results containing strain and micro crack distributions could then be upscaled to larger length scale by incorporating the effective material properties in respective material laws (e.g., reservoirs).

Data Availability Statement

The software package PACE3D was used for the generation of the simulation data sets. The software license can be purchased at Steinbeis Network (www.steinbeis.de) in the management of Britta Nestler and Michael Selzer under the subject area "Material Simulation and Process Optimization." The complete data set, on which this research article is based, can be accessed in the open-access repository at Späth et al. (2023).

Acknowledgments
Research has been initiated through funding of the project NE 822/34-1 and UR 64/17-1 of the German research foundation (DFG). The simulations and data analysis have been carried out within the MTET Program 38.04.04 of the Helmholtz association which is gratefully acknowledged. We thank the three anonymous reviewers and the associate editor for their constructive reviews. The authors acknowledge support by the state of Baden-Württemberg through bwHPC. Open Access funding enabled and organized by Projekt DEAL.

References

Abbona, F. (2003). Crystal Growth From Solutions. In k. Byrappa, T. Ohachi, M. Klapper, &, R. Fornari (Eds.), *International School on Crystal Growth of Technologically Important Electronic Materials* (pp. 89–117). Allied Publishers PVT. Limited, New Delhi, India.

Almansour, A., Laubach, S. E., Bickel, J. E., & Schultz, R. A. (2020). Value-of-information analysis of a fracture prediction method. *Society of Petroleum Engineers Reservoir Evaluation & Engineering*, *23*(03), 811–823. https://doi.org/10.2118/198906-pa

Ankit, K., Urai, J. L., & Nestler, B. (2015). Microstructural evolution in bitaxial crack-seal veins: A phase-field study. *Journal of Geophysical Research: Solid Earth*, *120*(5), 3096–3118. https://doi.org/10.1002/2015jb011934

Barrett, P., & Glennon, B. (2002). Characterizing the metastable zone width and solubility curve using Lasentec FBRM and PVM. *Chemical Engineering Research and Design*, *80*(7), 799–805. https://doi.org/10.1205/026387602320776876

Becker, S., Hilgers, C., Kukla, P. A., & Urai, J. L. (2011). Crack-seal microstructure evolution in bi-mineralic quartz–chlorite veins in shales and siltstones from the RWTH-1 well, Aachen, Germany. *Journal of Structural Geology*, *33*(4), 676–689. https://doi.org/10.1016/j.jsg.2011.01.001

Beckermann, C., Diepers, H.-J., Steinbach, I., Karma, A., & Tong, X. (1999). Modeling melt convection in phase-field simulations of solidification. *Journal of Computational Physics*, *154*(2), 468–496. https://doi.org/10.1006/jcph.1999.6323

Birkholzer, J. T., Zhou, Q., & Tsang, C.-F. (2009). Large-scale impact of CO_2 storage in deep saline aquifers: A sensitivity study on pressure response in stratified systems. *International Journal of Greenhouse Gas Control*, *3*(2), 181–194. https://doi.org/10.1016/j.ijggc.2008.08.002

Bons, P. D. (2001). Development of crystal morphology during unitaxial growth in a progressively widening vein: I. The numerical model. *Journal of Structural Geology*, *23*(6–7), 865–872. https://doi.org/10.1016/s0191-8141(00)00159-0

Bons, P. D., Elburg, M. A., & Gomez-Rivas, E. (2012). A review of the formation of tectonic veins and their microstructures. *Journal of Structural Geology*, *43*, 33–62. https://doi.org/10.1016/j.jsg.2012.07.005

Boullier, A.-M., & Robert, F. (1992). Paleoseismic events recorded in Archaean gold-quartz vein networks, Val d'Or, Abitibi, Quebec, Canada. *Journal of Structural Geology*, *14*(2), 161–179. https://doi.org/10.1016/0191-8141(92)90054-z

Bringedal, C., von Wolff, L., & Pop, I. S. (2020). Phase field modeling of precipitation and dissolution processes in porous media: Upscaling and numerical experiments. *Multiscale Modeling and Simulation*, *18*(2), 1076–1112. https://doi.org/10.1137/19m1239003

Busch, B., Okamoto, A., Garbev, K., & Hilgers, C. (2021). Experimental fracture sealing in reservoir sandstones and its relation to rock texture. *Journal of Structural Geology*, *153*, 104447. https://doi.org/10.1016/j.jsg.2021.104447

Cecil, C. B., & Heald, M. T. (1971). Experimental investigation of the effects of grain coatings on quartz growth. *Journal of Sedimentary Research*, *41*(2), 582–584. https://doi.org/10.1306/74d722e3-2b21-11d7-8648000102c1865d

Choquet, C., & Mikelić, A. (2009). Rigorous upscaling of the reactive flow with finite kinetics and under dominant Péclet number. *Continuum Mechanics and Thermodynamics*, *21*(2), 125–140. https://doi.org/10.1007/s00161-009-0099-z

Choudhury, A., & Nestler, B. (2012). Grand-potential formulation for multicomponent phase transformations combined with thin-interface asymptotics of the double-obstacle potential. *Physical Review E - Statistical Physics, Plasmas, Fluids, and Related Interdisciplinary Topics*, *85*(2), 021602. https://doi.org/10.1103/physreve.85.021602

Colombani, J. (2008). Measurement of the pure dissolution rate constant of a mineral in water. *Geochimica et Cosmochimica Acta*, *72*(23), 5634–5640. https://doi.org/10.1016/j.gca.2008.09.007

Cox, S. F. (2007). Structural and isotopic constraints on fluid flow regimes and fluid pathways during upper crustal deformation: An example from the Taemas area of the Lachlan Orogen, SE Australia. *Journal of Geophysical Research*, *112*(B8), 1–23. https://doi.org/10.1029/2006jb004734

Cox, S. F., Etheridge, M. A., & Wall, V. J. (1987). The role of fluids in syntectonic mass transport, and the localization of metamorphic vein-type ore deposits. *Ore Geology Reviews*, *2*(1–3), 65–86. https://doi.org/10.1016/0169-1368(87)90024-2

Cvetkovic, V., & Gotovac, H. (2014). On the upscaling of chemical transport in fractured rock. *Water Resources Research*, *50*(7), 5797–5816. https://doi.org/10.1002/2014wr015505

Daubner, S., Weichel, M., Schneider, D., & Nestler, B. (2022). Modeling intercalation in cathode materials with phase-field methods: Assumptions and implications using the example of LiFePO4. *Electrochimica Acta*, *421*, 140516. https://doi.org/10.1016/j.electacta.2022.140516

Deng, H., Poonoosamy, J., & Molins, S. (2022). A reactive transport modeling perspective on the dynamics of interface-coupled dissolution-precipitation. *Applied Geochemistry*, *137*, 105207. https://doi.org/10.1016/j.apgeochem.2022.105207

Fisher, D. M., & Brantley, S. L. (1992). Models of quartz overgrowth and vein formation: Deformation and episodic fluid flow in an ancient subduction zone. *Journal of Geophysical Research*, *97*(B13), 20043–20061. https://doi.org/10.1029/92jb01582

Gale, J. F. W., Lander, R. H., Reed, R. M., & Laubach, S. E. (2010). Modeling fracture porosity evolution in dolostone. *Journal of Structural Geology*, *32*(9), 1201–1211. https://doi.org/10.1016/j.jsg.2009.04.018

Guével, A., Rattez, H., & Veveakis, E. (2020). Viscous phase-field modeling for chemo-mechanical microstructural evolution: Application to geomaterials and pressure solution. *International Journal of Solids and Structures*, *207*, 230–249. https://doi.org/10.1016/j.ijsolstr.2020.09.026

Herman, J. S., & White, W. B. (1985). Dissolution kinetics of dolomite: Effects of lithology and fluid flow velocity. *Geochimica et Cosmochimica Acta*, *49*(10), 2017–2026. https://doi.org/10.1016/0016-7037(85)90060-2

Hilgers, C., Dilg-Gruschinski, K., & Urai, J. L. (2004). Microstructural evolution of syntaxial veins formed by advective flow. *Geology*, *32*(3), 261–264. https://doi.org/10.1130/g20024.1

Hilgers, C., Koehn, D., Bons, P. D., & Urai, J. L. (2001). Development of crystal morphology during unitaxial growth in a progressively widening vein: II. Numerical simulations of the evolution of antitaxial fibrous veins. *Journal of Structural Geology*, *23*(6–7), 873–885. https://doi.org/10.1016/s0191-8141(00)00160-7

Hilgers, C., & Urai, J. L. (2002). Experimental study of syntaxial vein growth during lateral fluid flow in transmitted light: First results. *Journal of Structural Geology*, *24*(6–7), 1029–1043. https://doi.org/10.1016/s0191-8141(01)00089-x

Hoffrogge, P. W., Mukherjee, A., Nani, E. S., Amos, P. G. K., Wang, F., Schneider, D., & Nestler, B. (2021). Multiphase-field model for surface diffusion and attachment kinetics in the grand-potential framework. *Physical Review E - Statistical Physics, Plasmas, Fluids, and Related Interdisciplinary Topics*, *103*(3), 033307. https://doi.org/10.1103/physreve.103.033307

Hötzer, J., Reiter, A., Hierl, H., Steinmetz, P., Selzer, M., & Nestler, B. (2018). The parallel multi-physics phase-field framework Pace3D. *Journal of Computational Science*, *26*, 1–12. https://doi.org/10.1016/j.jocs.2018.02.011

Hubert, J., Emmerich, H., & Urai, J. L. (2009). Modelling the evolution of vein microstructure with phase-field techniques–A first look. *Journal of Metamorphic Geology*, *27*(7), 523–530. https://doi.org/10.1111/j.1525-1314.2009.00839.x

Kling, T., Schwarz, J.-O., Wendler, F., Enzmann, F., & Blum, P. (2017). Fracture flow due to hydrothermally induced quartz growth. *Advances in Water Resources*, *107*, 93–107. https://doi.org/10.1016/j.advwatres.2017.06.011

Lander, R. H., Larese, R. E., & Bonnell, L. M. (2008). Toward more accurate quartz cement models: The importance of euhedral versus noneuhedral growth rates. *AAPG Bulletin*, *92*(11), 1537–1563. https://doi.org/10.1306/07160808037

Lander, R. H., & Laubach, S. E. (2015). Insights into rates of fracture growth and sealing from a model for quartz cementation in fractured sandstones. *GSA Bulletin*, *127*(3–4), 516–538. https://doi.org/10.1130/b31092.1

Laxmipathy, V. P., Wang, F., Selzer, M., Nestler, B., & Ankit, K. (2019). Influence of melt convection on the morphological evolution of seaweed structures: Insights from phase-field simulations. *Computational Materials Science*, *170*, 109196. https://doi.org/10.1016/j.commatsci.2019.109196

Le Borgne, T., Bolster, D., Dentz, M., de Anna, P., & Tartakovsky, A. (2011). Effective pore-scale dispersion upscaling with a correlated continuous time random walk approach. *Water Resources Research*, *47*(12), W12538. https://doi.org/10.1029/2011wr010457

Lee, Y.-J., & Morse, J. W. (1999). Calcite precipitation in synthetic veins: Implications for the time and fluid volume necessary for vein filling. *Chemical Geology*, *156*(1–4), 151–170. https://doi.org/10.1016/s0009-2541(98)00183-1

Lee, Y.-J., Morse, J. W., & Wiltschko, D. V. (1996). An experimentally verified model for calcite precipitation in veins. *Chemical Geology*, *130*(3–4), 203–215. https://doi.org/10.1016/0009-2541(96)00008-3

Li, L., Peters, C. A., & Celia, M. A. (2006). Upscaling geochemical reaction rates using pore-scale network modeling. *Advances in Water Resources*, *29*(9), 1351–1370. https://doi.org/10.1016/j.advwatres.2005.10.011

Li, L., Peters, C. A., & Celia, M. A. (2007). Effects of mineral spatial distribution on reaction rates in porous media. *Water Resources Research*, *43*(1), W01419. https://doi.org/10.1029/2005wr004848

Liu, Z., & Dreybrod, W. (1997). Dissolution kinetics of calcium carbonate minerals in $H_2O \cdot CO_2$ solutions in turbulent flow: The role of the diffusion boundary layer and the slow reaction $H_2O + CO_2 \rightarrow H^+ + HCO_3^-$. *Geochimica et Cosmochimica Acta*, *61*(14), 2879–2889. https://doi.org/10.1016/s0016-7037(97)00143-9

Mai, W., Soghrati, S., & Buchheit, R. G. (2016). A phase field model for simulating the pitting corrosion. *Corrosion Science*, *110*, 157–166. https://doi.org/10.1016/j.corsci.2016.04.001

McNamara, D. D., Lister, A., & Prior, D. J. (2016). Calcite sealing in a fractured geothermal reservoir: Insights from combined EBSD and chemistry mapping. *Journal of Volcanology and Geothermal Research*, *323*, 38–52. https://doi.org/10.1016/j.jvolgeores.2016.04.042

Mikelić, A., Devigne, V., & van Duijn, C. J. (2006). Rigorous upscaling of the reactive flow through a pore, under dominant Peclet and Damkohler numbers. *SIAM Journal on Mathematical Analysis*, *38*(4), 1262–1287. https://doi.org/10.1137/050633573

Moelans, N., Blanpain, B., & Wollants, P. (2008). An introduction to phase-field modeling of microstructure evolution. *Calphad*, *32*(2), 268–294. https://doi.org/10.1016/j.calphad.2007.11.003

Molins, S., Soulaine, C., Prasianakis, N. I., Abbasi, A., Poncet, P., Ladd, A. J. C., et al. (2020). Simulation of mineral dissolution at the pore scale with evolving fluid-solid interfaces: Review of approaches and benchmark problem set. *Computational Geosciences*, *25*(4), 1285–1318. https://doi.org/10.1007/s10596-019-09903-x

Molins, S., Trebotich, D., Miller, G. H., & Steefel, C. I. (2017). Mineralogical and transport controls on the evolution of porous media texture using direct numerical simulation. *Water Resources Research*, *53*(5), 3645–3661. https://doi.org/10.1002/2016wr020323

Nestler, B., & Choudhury, A. (2011). Phase-field modeling of multi-component systems. *Current Opinion in Solid State & Materials Science*, *15*(3), 93–105. https://doi.org/10.1016/j.cossms.2011.01.003

Nestler, B., Garcke, H., & Stinner, B. (2005). Multicomponent alloy solidification: Phase-field modeling and simulations. *Physical Review E*, *71*(4), 041609. https://doi.org/10.1103/physreve.71.041609

Nollet, S., Hilgers, C., & Urai, J. L. (2006). Experimental study of polycrystal growth from an advecting supersaturated fluid in a model fracture. *Geofluids*, *6*(2), 185–200. https://doi.org/10.1111/j.1468-8123.2006.00142.x

Nollet, S., Urai, J. L., Bons, P. D., & Hilgers, C. (2005). Numerical simulations of polycrystal growth in veins. *Journal of Structural Geology*, *27*(2), 217–230. https://doi.org/10.1016/j.jsg.2004.10.003

Okamoto, A., Saishu, H., Hirano, N., & Tsuchiya, N. (2010). Mineralogical and textural variation of silica minerals in hydrothermal flow-through experiments: Implications for quartz vein formation. *Geochimica et Cosmochimica Acta*, *74*(13), 3692–3706. https://doi.org/10.1016/j.gca.2010.03.031

Okamoto, A., & Sekine, K. (2011). Textures of syntaxial quartz veins synthesized by hydrothermal experiments. *Journal of Structural Geology*, *33*(12), 1764–1775. https://doi.org/10.1016/j.jsg.2011.10.004

Opdyke, B. N., Gust, G., & Ledwell, J. R. (1987). Mass transfer from smooth alabaster surfaces in turbulent flows. *Geophysical Research Letters*, *14*(11), 1131–1134. https://doi.org/10.1029/gl014i011p01131

Painter, S., Cvetkovic, V., Mancillas, J., & Pensado, O. (2008). Time domain particle tracking methods for simulating transport with retention and first-order transformation. *Water Resources Research*, *44*(1), W01406. https://doi.org/10.1029/2007wr005944

Prajapati, N., Abad Gonzalez, A., Selzer, M., Nestler, B., Busch, B., & Hilgers, C. (2020). Quartz cementation in polycrystalline sandstone: Insights from phase-field simulations. *Journal of Geophysical Research: Solid Earth*, *125*(2), e2019JB019137. https://doi.org/10.1029/2019jb019137

Prajapati, N., Herrmann, C., Späth, M., Schneider, D., Selzer, M., & Nestler, B. (2020). Brittle anisotropic fracture propagation in quartz sandstone: Insights from phase-field simulations. *Computational Geosciences*, *24*(3), 1361–1376. https://doi.org/10.1007/s10596-020-09956-3

Prajapati, N., Selzer, M., & Nestler, B. (2017). Computational modeling of calcite cementation in saline limestone aquifers: A phase-field study. *Geothermal Energy*, *5*(1), 1–18. https://doi.org/10.1186/s40517-017-0072-1

Prajapati, N., Selzer, M., Nestler, B., Busch, B., & Hilgers, C. (2018). Modeling fracture cementation processes in calcite limestone: A phase-field study. *Geothermal Energy*, *6*(1), 1–15. https://doi.org/10.1186/s40517-018-0093-4

Prajapati, N., Selzer, M., Nestler, B., Busch, B., Hilgers, C., & Ankit, K. (2018). Three-dimensional phase-field investigation of pore space cementation and permeability in quartz sandstone. *Journal of Geophysical Research: Solid Earth*, *123*(8), 6378–6396. https://doi.org/10.1029/2018jb015618

Prajapati, N., Späth, M., Knecht, L., Selzer, M., & Nestler, B. (2021). Quantitative phase-field modeling of faceted crystal dissolution processes. *Crystal Growth & Design*, *21*(6), 3266–3279. https://doi.org/10.1021/acs.cgd.0c01715

Prasianakis, N. I., Gatschet, M., Abbasi, A., & Churakov, S. V. (2018). Upscaling strategies of porosity-permeability correlations in reacting environments from pore-scale simulations. *Geofluids*, *2018*, 9260603. https://doi.org/10.1155/2018/9260603

Ramsay, J. G. (1980). The crack–seal mechanism of rock deformation. *Nature*, *284*(5752), 135–139. https://doi.org/10.1038/284135a0

Ray, N., Oberlander, J., & Frolkovic, P. (2019). Numerical investigation of a fully coupled micro-macro model for mineral dissolution and precipitation. *Computational Geosciences*, *23*(5), 1173–1192. https://doi.org/10.1007/s10596-019-09876-x

Redeker, M., Rohde, C., & Sorin Pop, I. (2016). Upscaling of a tri-phase phase-field model for precipitation in porous media. *IMA Journal of Applied Mathematics*, *81*(5), 898–939. https://doi.org/10.1093/imamat/hxw023

Reder, M., Hoffrogge, P. W., Schneider, D., & Nestler, B. (2022). A phase-field based model for coupling two-phase flow with the motion of immersed rigid bodies. *International Journal for Numerical Methods in Engineering*, *123*(16), 3757–3780. https://doi.org/10.1002/nme.6988

Reder, M., Schneider, D., Wang, F., Daubner, S., & Nestler, B. (2021). Phase-field formulation of a fictitious domain method for particulate flows interacting with complex and evolving geometries. *International Journal for Numerical Methods in Fluids*, *93*(8), 2486–2507. https://doi.org/10.1002/fld.4984

Rutqvist, J. (2012). The geomechanics of CO_2 storage in deep sedimentary formations. *Geotechnical & Geological Engineering*, *30*(3), 525–551. https://doi.org/10.1007/s10706-011-9491-0

Schoof, E., Herrmann, C., Streichhan, N., Selzer, M., Schneider, D., & Nestler, B. (2019). On the multiphase-field modeling of martensitic phase transformation in dual-phase steel using J2-viscoplasticity. *Modelling and Simulation in Materials Science and Engineering*, *27*(2), 025010. https://doi.org/10.1088/1361-651x/aaf980

Schoof, E., Schneider, D., Streichhan, N., Mittnacht, T., Selzer, M., & Nestler, B. (2018). Multiphase-field modeling of martensitic phase transformation in a dual-phase microstructure. *International Journal of Solids and Structures*, *134*, 181–194. https://doi.org/10.1016/j.ijsolstr.2017.10.032

Sibson, R. H., Moore, J. M. M., & Rankin, A. H. (1975). Seismic pumping—A hydrothermal fluid transport mechanism. *Journal of the Geological Society*, *131*(6), 653–659. https://doi.org/10.1144/gsjgs.131.6.0653

Sibson, R. H., Robert, F., & Poulsen, K. H. (1988). High-angle reverse faults, fluid-pressure cycling, and mesothermal gold-quartz deposits. *Geology*, *16*(6), 551–555. https://doi.org/10.1130/0091-7613(1988)016<0551:harffp>2.3.co;2

Singurindy, O., & Berkowitz, B. (2005). The role of fractures on coupled dissolution and precipitation patterns in carbonate rocks. *Advances in Water Resources*, *28*(5), 507–521. https://doi.org/10.1016/j.advwatres.2005.01.002

Soulaine, C., & Tchelepi, H. A. (2016). Micro-continuum approach for pore-scale simulation of subsurface processes. *Transport in Porous Media*, *113*(3), 431–456. https://doi.org/10.1007/s11242-016-0701-3

Späth, M., Selzer, M., Busch, B., Schneider, D., Hilgers, C., Urai, J. L., & Nestler, B. (2023). Data set for phase-field simulation of epitaxial crystal growth in open fractures with lateral flow [Dataset]. Zenodo. https://doi.org/10.5281/zenodo.7516287

Späth, M., Spruženiece, L., Urai, J. L., Selzer, M., Arndt, M., & Nestler, B. (2021). Kinematics of crystal growth in single-seal syntaxial veins in limestone-A phase-field study. *Journal of Geophysical Research: Solid Earth*, *126*(10), e2021JB022106. https://doi.org/10.1029/2021jb022106

Späth, M., Urai, J. L., & Nestler, B. (2022a). Formation of radiator structures in quartz veins - Phase-field modeling of multi-crack sealing. *Journal of Structural Geology*, *158*, 104576. https://doi.org/10.1016/j.jsg.2022.104576

Späth, M., Urai, J. L., & Nestler, B. (2022b). Incomplete crack sealing causes localization of fracturing in hydrothermal quartz veins. *Geophysical Research Letters*, *49*(15), e2022GL098643. https://doi.org/10.1029/2022gl098643

Spruženiece, L., Späth, M., Urai, J. L., Ukar, E., Selzer, M., & Nestler, B. (2021). Wide-blocky veins explained by dependency of crystal growth rate on fracture surface type: Insights from phase-field modeling. *Geology*, *49*(6), 641–646. https://doi.org/10.1130/g48472.1

Spruženiece, L., Späth, M., Urai, J. L., Ukar, E., Selzer, M., Nestler, B., & Schwedt, A. (2020). Formation of wide-blocky calcite veins by extreme growth competition. *Journal of the Geological Society*, *178*(2), 1–17. https://doi.org/10.1144/jgs2020-104

Steefel, C. I. (2019). Reactive transport at the crossroads. *Reviews in Mineralogy and Geochemistry*, *85*(1), 1–26. https://doi.org/10.2138/rmg.2019.85.1

Steefel, C. I., Appelo, C. A. J., Arora, B., Jacques, D., Kalbacher, T., Kolditz, O., et al. (2015). Reactive transport codes for subsurface environmental simulation. *Computational Geosciences*, *19*(3), 445–478. https://doi.org/10.1007/s10596-014-9443-x

Steefel, C. I., Molins, S., & Trebotich, D. (2013). Pore scale processes associated with subsurface CO_2 injection and sequestration. *Reviews in Mineralogy and Geochemistry*, *77*(1), 259–303. https://doi.org/10.2138/rmg.2013.77.8

Steinbach, I. (2009). Phase-field models in materials science. *Modelling and Simulation in Materials Science and Engineering*, *17*(7), 073001. https://doi.org/10.1088/0965-0393/17/7/073001

Steinbach, I. (2013). Phase-field model for microstructure evolution at the mesoscopic scale. *Annual Review of Materials Research*, *43*(1), 89–107. https://doi.org/10.1146/annurev-matsci-071312-121703

Steinmetz, P., Hötzer, J., Kellner, M., Genau, A., & Nestler, B. (2018). Study of pattern selection in 3D phase-field simulations during the directional solidification of ternary eutectic Al-Ag-Cu. *Computational Materials Science*, *148*, 131–140. https://doi.org/10.1016/j.commatsci.2018.02.040

Tartakovsky, A. M., Meakin, P., Scheibe, T. D., & Eichler West, R. M. (2007). Simulations of reactive transport and precipitation with smoothed particle hydrodynamics. *Journal of Computational Physics*, *222*(2), 654–672. https://doi.org/10.1016/j.jcp.2006.08.013

Thomas, L. A., Wooster, N., & Wooster, W. A. (1949). The hydrothermal synthesis of quartz. *Discussions of the Faraday Society*, *5*, 341–345. https://doi.org/10.1039/df9490500341

Urai, J. L., Williams, P. F., & Van Roermund, H. L. M. (1991). Kinematics of crystal growth in syntectonic fibrous veins. *Journal of Structural Geology*, *13*(7), 823–836. https://doi.org/10.1016/0191-8141(91)90007-6

Viswanathan, H. S., Ajo-Franklin, J., Birkholzer, J. T., Carey, J. W., Guglielmi, Y., Hyman, J. D., et al. (2022). From fluid flow to coupled processes in fractured rock: Recent advances and new frontiers. *Reviews of Geophysics*, *60*(1), e2021RG000744. https://doi.org/10.1029/2021rg000744

Wendler, F., Okamoto, A., & Blum, P. (2016). Phase-field modeling of epitaxial growth of polycrystalline quartz veins in hydrothermal experiments. *Geofluids*, *16*(2), 211–230. https://doi.org/10.1111/gfl.12144

Xu, Z., Huang, H., Li, X., & Meakin, P. (2012). Phase field and level set methods for modeling solute precipitation and/or dissolution. *Computer Physics Communications*, *183*(1), 15–19. https://doi.org/10.1016/j.cpc.2011.08.005

Xu, Z., & Meakin, P. (2008). Phase-field modeling of solute precipitation and dissolution. *The Journal of Chemical Physics*, *129*(1), 014705. https://doi.org/10.1063/1.2948949

Yamashita, R., & Kimura, H. (1990). Particle-tracking technique for nuclide decay chain transport in fractured porous media. *Journal of Nuclear Science and Technology*, *27*(11), 1041–1049. https://doi.org/10.1080/18811248.1990.9731289

Zhang, H., Wu, Y., Wang, F., Guo, F., & Nestler, B. (2021). Phase-field modeling of multiple emulsions via spinodal decomposition. *Langmuir*, *37*(17), 5275–5281. https://doi.org/10.1021/acs.langmuir.1c00275

Zhang, J., & Adams, J. B. (2002). FACET: A novel model of simulation and visualization of polycrystalline thin film growth. *Modelling and Simulation in Materials Science and Engineering*, *10*(4), 381–401. https://doi.org/10.1088/0965-0393/10/4/302